VERSITA

OPTO-ELECTRONICS REVIEW **20**(3), 279–308

DOI: 10.2478/s11772-012-0037-7

History of infrared detectors

A. ROGALSKI*

Institute of Applied Physics, Military University of Technology, 2 Kaliskiego Str., 00–908 Warsaw, Poland

This paper overviews the history of infrared detector materials starting with Herschel's experiment with thermometer on February 11th, 1800. Infrared detectors are in general used to detect, image, and measure patterns of the thermal heat radiation which all objects emit. At the beginning, their development was connected with thermal detectors, such as thermocouples and bolometers, which are still used today and which are generally sensitive to all infrared wavelengths and operate at room temperature. The second kind of detectors, called the photon detectors, was mainly developed during the 20th Century to improve sensitivity and response time. These detectors have been extensively developed since the 1940's. Lead sulphide (PbS) was the first practical IR detector with sensitivity to infrared wavelengths up to ~3 μm. After World War II infrared detector technology development was and continues to be primarily driven by military applications. Discovery of variable band gap HgCdTe ternary alloy by Lawson and co-workers in 1959 opened a new area in IR detector technology and has provided an unprecedented degree of freedom in infrared detector design. Many of these advances were transferred to IR astronomy from Departments of Defence research. Later on civilian applications of infrared technology are frequently called "dual-use technology applications." One should point out the growing utilisation of IR technologies in the civilian sphere based on the use of new materials and technologies, as well as the noticeable price decrease in these high cost technologies. In the last four decades different types of detectors are combined with electronic readouts to make detector focal plane arrays (FPAs). Development in FPA technology has revolutionized infrared imaging. Progress in integrated circuit design and fabrication techniques has resulted in continued rapid growth in the size and performance of these solid state arrays.

Keywords: thermal and photon detectors, lead salt detectors, HgCdTe detectors, microbolometers, focal plane arrays.

Contents

1. Introduction

Looking back over the past 1000 years we notice that infrared radiation (IR) itself was unknown until 212 years ago when Herschel's experiment with thermometer and prism was first reported. Frederick William Herschel (1738–1822) was born in Hanover, Germany but emigrated to Britain at age 19, where he became well known as both a musician and an astronomer. Herschel became most famous for the discovery of Uranus in 1781 (the first new planet found since antiquity) in addition to two of its major moons, Titania and Oberon. He also discovered two moons of Saturn and infrared radiation. Herschel is also known for the twenty-four symphonies that he composed.

W. Herschel made another milestone discovery – discovery of infrared light on February 11th, 1800. He studied the spectrum of sunlight with a prism [see Fig. 1 in Ref. 1], measuring temperature of each colour. The detector consisted of liquid in a glass thermometer with a specially blackened bulb to absorb radiation. Herschel built a crude monochromator that used a thermometer as a detector, so that he could measure the distribution of energy in sunlight and found that the highest temperature was just beyond the red, what we now call the infrared ('below the red', from the Latin 'infra' – be-

*e-mail: rogan@wat.edu.pl

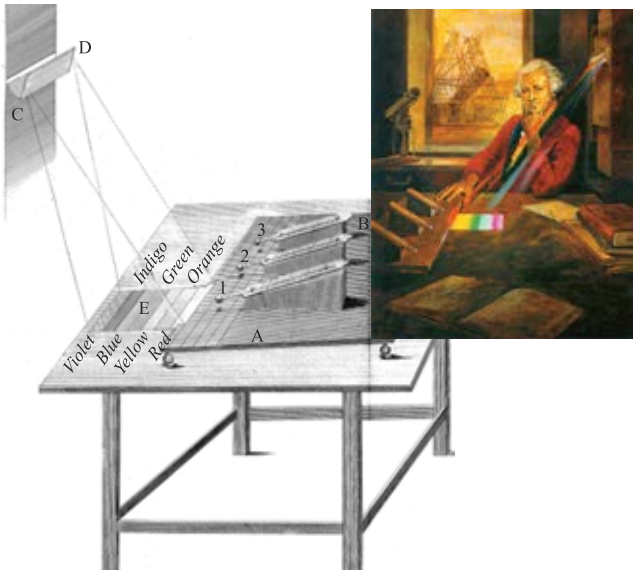

Fig. 1. Herschel's first experiment: A,B – the small stand, 1,2,3 – the thermometers upon it, C,D – the prism at the window, E – the spectrum thrown upon the table, so as to bring the last quarter of an inch of the read colour upon the stand (after Ref. 1). Inside Sir Frederick William Herschel (1738–1822) measures infrared light from the sun – artist's impression (after Ref. 2).

low) – see Fig. 1(b) [2]. In April 1800 he reported it to the Royal Society as dark heat (Ref. 1, pp. 288–290):

> *Here the thermometer No. 1 rose 7 degrees, in 10 minutes, by an exposure to the full red coloured rays. I drew back the stand, till the centre of the ball of No. 1 was just at the vanishing of the red colour, so that half its ball was within, and half without, the visible rays of the sun... And here the thermometer No. 1 rose, in 16 minutes,* $8\frac{3}{4}$ *degrees, when its centre was* $\frac{1}{2}$ *inch out of the visible rays of the sun. Now, as before we had a rising of 9 degrees, and here* $8\frac{3}{4}$ *the difference is almost too trifling to suppose, that this latter situation of the thermometer was much beyond the maximum of the heating power; while, at the same time, the experiment sufficiently indicates, that the place inquired after need not be looked for at a greater distance.*

Making further experiments on what Herschel called the 'calorific rays' that existed beyond the red part of the spectrum, he found that they were reflected, refracted, absorbed and transmitted just like visible light [1,3,4].

The early history of IR was reviewed about 50 years ago in three well-known monographs [5–7]. Many historical information can be also found in four papers published by Barr [3,4,8,9] and in more recently published monograph [10]. Table 1 summarises the historical development of infrared physics and technology [11,12].

2. Historical perspective

For thirty years following Herschel's discovery, very little progress was made beyond establishing that the infrared radiation obeyed the simplest laws of optics. Slow progress in the study of infrared was caused by the lack of sensitive and accurate detectors – the experimenters were handicapped by the ordinary thermometer. However, towards the second decade of the 19th century, Thomas Johann Seebeck began to examine the junction behaviour of electrically conductive materials. In 1821 he discovered that a small electric current will flow in a closed circuit of two dissimilar metallic conductors, when their junctions are kept at different temperatures [13]. During that time, most physicists thought that radiant heat and light were different phenomena, and the discovery of Seebeck indirectly contributed to a revival of the debate on the nature of heat. Due to small output vol- tage of Seebeck's junctions, some μV/K, the measurement of very small temperature differences were prevented. In 1829 L. Nobili made the first thermocouple and improved electrical thermometer based on the thermoelectric effect discovered by Seebeck in 1826. Four years later, M. Melloni introduced the idea of connecting several bismuth-copper thermocouples in series, generating a higher and, therefore, measurable output voltage. It was at least 40 times more sensitive than the best thermometer available and could detect the heat from a person at a distance of 30 ft [8]. The output voltage of such a thermopile structure linearly increases with the number of connected thermocouples. An example of thermopile's prototype invented by Nobili is shown in Fig. 2(a). It consists of twelve large bismuth and antimony elements. The elements were placed upright in a brass ring secured to an adjustable support, and were screened by a wooden disk with a 15-mm central aperture. Incomplete version of the Nobili-Melloni thermopile originally fitted with the brass cone-shaped tubes to collect ra- diant heat is shown in Fig. 2(b). This instrument was much more sensitive than the thermometers previously used and became the most widely used detector of IR radiation for the next half century.

The third member of the trio, Langley's bolometer appeared in 1880 [7]. Samuel Pierpont Langley (1834–1906) used two thin ribbons of platinum foil connected so as to form two arms of a Wheatstone bridge (see Fig. 3) [15]. This instrument enabled him to study solar irradiance far into its infrared region and to measure the intensity of solar radiation at various wavelengths [9,16,17]. The bolometer's sen-

(a) (b)

Fig. 2 . The Nobili-Meloni thermopiles: (a) thermopile's prototype invented by Nobili (ca. 1829), (b) incomplete version of the Nobili--Melloni thermopile (ca. 1831). Museo Galileo – Institute and Museum of the History of Science, Piazza dei Giudici 1, 50122 Florence, Italy (after Ref. 14).

Table 1. Milestones in the development of infrared physics and technology (up-dated after Refs. 11 and 12)

Year	Event
1800	Discovery of the existence of thermal radiation in the invisible beyond the red by W. HERSCHEL
1821	Discovery of the thermoelectric effects using an antimony-copper pair by T.J. SEEBECK
1830	Thermal element for thermal radiation measurement by L. NOBILI
1833	Thermopile consisting of 10 in-line Sb-Bi thermal pairs by L. NOBILI and M. MELLONI
1834	Discovery of the PELTIER effect on a current-fed pair of two different conductors by J.C. PELTIER
1835	Formulation of the hypothesis that light and electromagnetic radiation are of the same nature by A.M. AMPERE
1839	Solar absorption spectrum of the atmosphere and the role of water vapour by M. MELLONI
1840	Discovery of the three atmospheric windows by J. HERSCHEL (son of W. HERSCHEL)
1857	Harmonization of the three thermoelectric effects (SEEBECK, PELTIER, THOMSON) by W. THOMSON (Lord KELVIN)
1859	Relationship between absorption and emission by G. KIRCHHOFF
1864	Theory of electromagnetic radiation by J.C. MAXWELL
1873	Discovery of photoconductive effect in selenium by W. SMITH
1876	Discovery of photovoltaic effect in selenium (photopiles) by W.G. ADAMS and A.E. DAY
1879	Empirical relationship between radiation intensity and temperature of a blackbody by J. STEFAN
1880	Study of absorption characteristics of the atmosphere through a Pt bolometer resistance by S.P. LANGLEY
1883	Study of transmission characteristics of IR-transparent materials by M. MELLONI
1884	Thermodynamic derivation of the STEFAN law by L. BOLTZMANN
1887	Observation of photoelectric effect in the ultraviolet by H. HERTZ
1890	J. ELSTER and H. GEITEL constructed a photoemissive detector consisted of an alkali-metal cathode
1894, 1900	Derivation of the wavelength relation of blackbody radiation by J.W. RAYEIGH and W. WIEN
1900	Discovery of quantum properties of light by M. PLANCK
1903	Temperature measurements of stars and planets using IR radiometry and spectrometry by W.W. COBLENTZ
1905	A. EINSTEIN established the theory of photoelectricity
1911	R. ROSLING made the first television image tube on the principle of cathode ray tubes constructed by F. Braun in 1897
1914	Application of bolometers for the remote exploration of people and aircrafts (a man at 200 m and a plane at 1000 m)
1917	T.W. CASE developed the first infrared photoconductor from substance composed of thallium and sulphur
1923	W. SCHOTTKY established the theory of dry rectifiers
1925	V.K. ZWORYKIN made a television image tube (kinescope) then between 1925 and 1933, the first electronic camera with the aid of converter tube (iconoscope)
1928	Proposal of the idea of the electro-optical converter (including the multistage one) by G. HOLST, J.H. DE BOER, M.C. TEVES, and C.F. VEENEMANS
1929	L.R. KOHLER made a converter tube with a photocathode (Ag/O/Cs) sensitive in the near infrared
1930	IR direction finders based on PbS quantum detectors in the wavelength range 1.5–3.0 μm for military applications (GUDDEN, GÖRLICH and KUTSCHER), increased range in World War II to 30 km for ships and 7 km for tanks (3–5 μm)
1934	First IR image converter
1939	Development of the first IR display unit in the United States (Sniperscope, Snooperscope)
1941	R.S. OHL observed the photovoltaic effect shown by a p-n junction in a silicon
1942	G. EASTMAN (Kodak) offered the first film sensitive to the infrared
1947	Pneumatically acting, high-detectivity radiation detector by M.J.E. GOLAY
1954	First imaging cameras based on thermopiles (exposure time of 20 min per image) and on bolometers (4 min)
1955	Mass production start of IR seeker heads for IR guided rockets in the US (PbS and PbTe detectors, later InSb detectors for Sidewinder rockets)
1957	Discovery of HgCdTe ternary alloy as infrared detector material by W.D. LAWSON, S. NELSON, and A.S. YOUNG
1961	Discovery of extrinsic Ge:Hg and its application (linear array) in the first LWIR FLIR systems
1965	Mass production start of IR cameras for civil applications in Sweden (single-element sensors with optomechanical scanner: AGA Thermografiesystem 660)
1970	Discovery of charge-couple device (CCD) by W.S. BOYLE and G.E. SMITH
1970	Production start of IR sensor arrays (monolithic Si-arrays: R.A. SOREF 1968; IR-CCD: 1970; SCHOTTKY diode arrays: F.D. SHEPHERD and A.C. YANG 1973; IR-CMOS: 1980; SPRITE: T. ELIOTT 1981)
1975	Lunch of national programmes for making spatially high resolution observation systems in the infrared from multielement detectors integrated in a mini cooler (so-called first generation systems): common module (CM) in the United States, thermal imaging common module (TICM) in Great Britain, syteme modulaire termique (SMT) in France
1975	First In bump hybrid infrared focal plane array
1977	Discovery of the broken-gap type-II InAs/GaSb superlattices by G.A. SAI-HALASZ, R. TSU, and L. ESAKI
1980	Development and production of second generation systems [cameras fitted with hybrid HgCdTe(InSb)/Si(readout) FPAs]. First demonstration of two-colour back-to-back SWIR GaInAsP detector by J.C. CAMPBELL, A.G. DENTAI, T.P. LEE, and C.A. BURRUS
1985	Development and mass production of cameras fitted with Schottky diode FPAs (platinum silicide)
1990	Development and production of quantum well infrared photoconductor (QWIP) hybrid second generation systems
1995	Production start of IR cameras with uncooled FPAs (focal plane arrays; microbolometer-based and pyroelectric)
2000	Development and production of third generation infrared systems

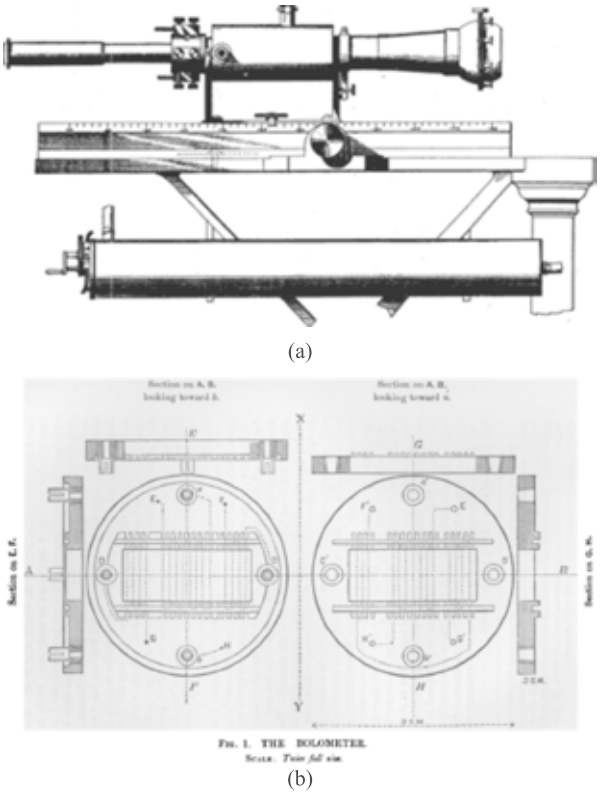

(a)

(b)

Fig. 3. Longley's bolometer (a) composed of two sets of thin platinum strips (b), a Wheatstone bridge, a battery, and a galvanometer measuring electrical current (after Ref. 15 and 16).

sitivity was much greater than that of contemporary thermopiles which were little improved since their use by Melloni. Langley continued to develop his bolometer for the next 20 years (400 times more sensitive than his first efforts). His latest bolometer could detect the heat from a cow at a distance of quarter of mile [9].

From the above information results that at the beginning the development of the IR detectors was connected with thermal detectors. The first photon effect, photoconductive effect, was discovered by Smith in 1873 when he experimented with selenium as an insulator for submarine cables [18]. This discovery provided a fertile field of investigation for several decades, though most of the efforts were of doubtful quality. By 1927, over 1500 articles and 100 patents were listed on photosensitive selenium [19]. It should be mentioned that the literature of the early 1900's shows increasing interest in the application of infrared as solution to numerous problems [7]. A special contribution of William Coblenz (1873–1962) to infrared radiometry and spectroscopy is marked by huge bibliography containing hundreds of scientific publications, talks, and abstracts to his credit [20,21]. In 1915, W. Coblentz at the US National Bureau of Standards develops thermopile detectors, which he uses to measure the infrared radiation from 110 stars. However, the low sensitivity of early infrared instruments prevented the detection of other near-IR sources. Work in infrared astronomy remained at a low level until breakthroughs in the development of new, sensitive infrared detectors were achieved in the late 1950's.

The principle of photoemission was first demonstrated in 1887 when Hertz discovered that negatively charged particles were emitted from a conductor if it was irradiated with ultraviolet [22]. Further studies revealed that this effect could be produced with visible radiation using an alkali metal electrode [23].

Rectifying properties of semiconductor-metal contact were discovered by Ferdinand Braun in 1874 [24], when he probed a naturally-occurring lead sulphide (galena) crystal with the point of a thin metal wire and noted that current flowed freely in one direction only. Next, Jagadis Chandra Bose demonstrated the use of galena-metal point contact to detect millimetre electromagnetic waves. In 1901 he filed a U.S patent for a point-contact semiconductor rectifier for detecting radio signals [25]. This type of contact called cat's whisker detector (sometimes also as crystal detector) played serious role in the initial phase of radio development. However, this contact was not used in a radiation detector for the next several decades. Although crystal rectifiers allowed to fabricate simple radio sets, however, by the mid-1920s the predictable performance of vacuum-tubes replaced them in most radio applications.

The period between World Wars I and II is marked by the development of photon detectors and image converters and by emergence of infrared spectroscopy as one of the key analytical techniques available to chemists. The image converter, developed on the eve of World War II, was of tremendous interest to the military because it enabled man to see in the dark.

The first IR photoconductor was developed by Theodore W. Case in 1917 [26]. He discovered that a substance composed of thallium and sulphur (Tl_2S) exhibited photoconductivity. Supported by the US Army between 1917 and 1918, Case adapted these relatively unreliable detectors for use as sensors in an infrared signalling device [27]. The prototype signalling system, consisting of a 60-inch diameter searchlight as the source of radiation and a thallous sulphide detector at the focus of a 24-inch diameter paraboloid mirror, sent messages 18 miles through what was described as 'smoky atmosphere' in 1917. However, instability of resistance in the presence of light or polarizing voltage, loss of responsivity due to over-exposure to light, high noise, sluggish response and lack of reproducibility seemed to be inherent weaknesses. Work was discontinued in 1918; communication by the detection of infrared radiation appeared distinctly unpromising. Later Case found that the addition of oxygen greatly enhanced the response [28].

The idea of the electro-optical converter, including the multistage one, was proposed by Holst *et al*. in 1928 [29]. The first attempt to make the converter was not successful. A working tube consisted of a photocathode in close proximity to a fluorescent screen was made by the authors in 1934 in Philips firm.

In about 1930, the appearance of the Cs-O-Ag phototube, with stable characteristics, to great extent discouraged further development of photoconductive cells until about 1940. The Cs-O-Ag photocathode (also called S-1) elabo-

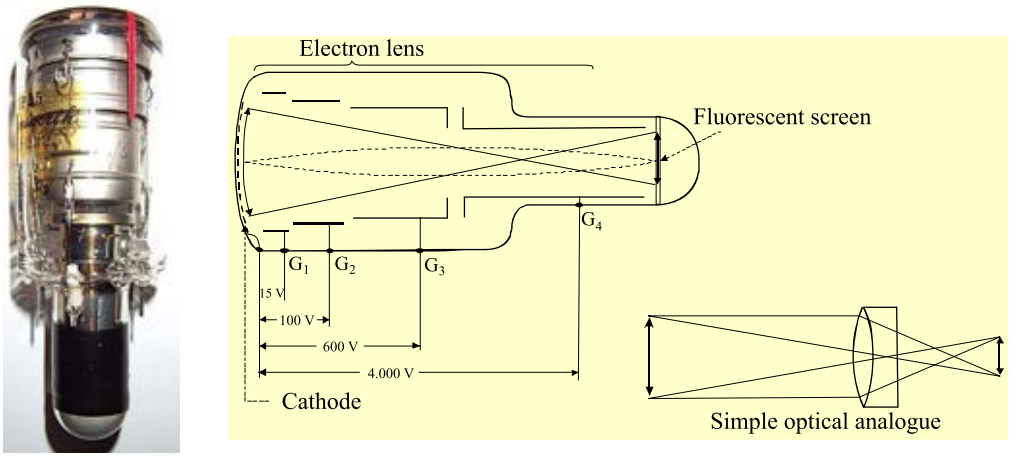

(a) (b)

Fig. 4. The original 1P25 image converter tube developed by the RCA (a). This device measures 115×38 mm overall and has 7 pins. It operation is indicated by the schematic drawing (b).

rated by Koller and Campbell [30] had a quantum efficiency two orders of magnitude above anything previously studied, and consequently a new era in photoemissive devices was inaugurated [31]. In the same year, the Japanese scientists S. Asao and M. Suzuki reported a method for enhancing the sensitivity of silver in the S-1 photocathode [32]. Consisted of a layer of caesium on oxidized silver, S-1 is sensitive with useful response in the near infrared, out to approximately 1.2 μm, and the visible and ultraviolet region, down to 0.3 μm. Probably the most significant IR development in the United States during 1930's was the Radio Corporation of America (RCA) IR image tube. During World War II, near-IR (NIR) cathodes were coupled to visible phosphors to provide a NIR image converter. With the establishment of the National Defence Research Committee, the development of this tube was accelerated. In 1942, the tube went into production as the RCA 1P25 image converter (see Fig. 4). This was one of the tubes used during World War II as a part of the "Snooperscope" and "Sniperscope," which were used for night observation with infrared sources of illumination. Since then various photocathodes have been developed including bialkali photocathodes for the visible region, multialkali photocathodes with high sensitivity extending to the infrared region and alkali halide photocathodes intended for ultraviolet detection.

The early concepts of image intensification were not basically different from those today. However, the early devices suffered from two major deficiencies: poor photocathodes and poor coupling. Later development of both cathode and coupling technologies changed the image intensifier into much more useful device. The concept of image intensification by cascading stages was suggested independently by number of workers. In Great Britain, the work was directed toward proximity focused tubes, while in the United State and in Germany – to electrostatically focused tubes. A history of night vision imaging devices is given by Biberman and Sendall in monograph *Electro-Optical Imaging: System Performance and Modelling*, SPIE Press, 2000 [10]. The Biberman's monograph describes the basic trends of infrared optoelectronics development in the USA, Great Britain, France, and Germany. Seven years later Ponomarenko and Filachev completed this monograph writing the book *Infrared Techniques and Electro-Optics in Russia: A History 1946-2006*, SPIE Press, about achievements of IR techniques and electrooptics in the former USSR and Russia [33].

In the early 1930's, interest in improved detectors began in Germany [27,34,35]. In 1933, Edgar W. Kutzscher at the University of Berlin, discovered that lead sulphide (from natural galena found in Sardinia) was photoconductive and had response to about 3 μm. B. Gudden at the University of Prague used evaporation techniques to develop sensitive PbS films. Work directed by Kutzscher, initially at the University of Berlin and later at the Electroacustic Company in Kiel, dealt primarily with the chemical deposition approach to film formation. This work ultimately lead to the fabrication of the most sensitive German detectors. These works were, of course, done under great secrecy and the results were not generally known until after 1945. Lead sulphide photoconductors were brought to the manufacturing stage of development in Germany in about 1943. Lead sulphide was the first practical infrared detector deployed in a variety of applications during the war. The most notable was the Kiel IV, an airborne IR system that had excellent range and which was produced at Carl Zeiss in Jena under the direction of Werner K. Weihe [6].

In 1941, Robert J. Cashman improved the technology of thallous sulphide detectors, which led to successful production [36,37]. Cashman, after success with thallous sulphide detectors, concentrated his efforts on lead sulphide detectors, which were first produced in the United States at Northwestern University in 1944. After World War II Cashman found that other semiconductors of the lead salt family (PbSe and PbTe) showed promise as infrared detectors [38]. The early detector cells manufactured by Cashman are shown in Fig. 5.

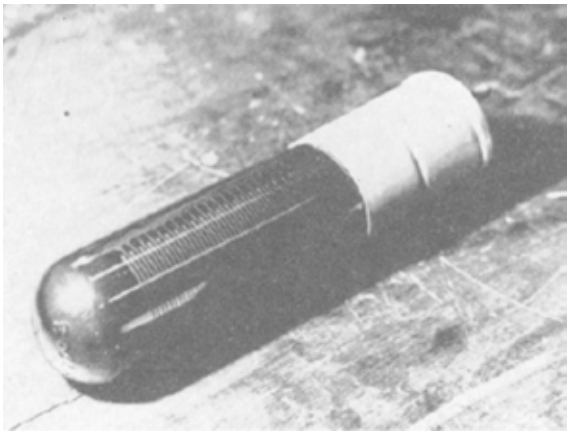

(a)

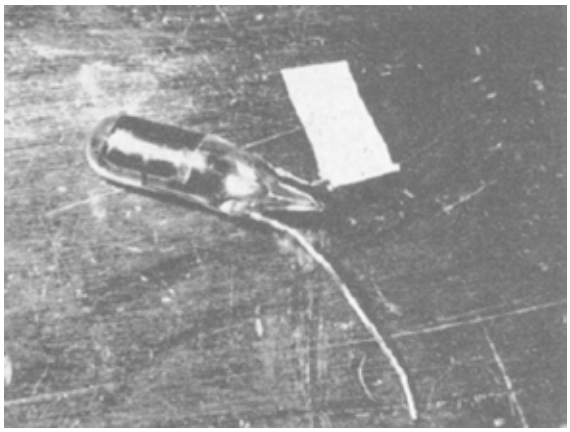

(b)

Fig. 5. Cashman's detector cells: (a) Tl_2S cell (ca. 1943): a grid of two intermeshing comb-line sets of conducting paths were first provided and next the T_2S was evaporated over the grid structure; (b) PbS cell (ca. 1945) the PbS layer was evaporated on the wall of the tube on which electrical leads had been drawn with aquadag (after Ref. 38).

After 1945, the wide-ranging German trajectory of research was essentially the direction continued in the USA, Great Britain and Soviet Union under military sponsorship after the war [27,39]. Kutzscher's facilities were captured by the Russians, thus providing the basis for early Soviet detector development. From 1946, detector technology was rapidly disseminated to firms such as Mullard Ltd. in Southampton, UK, as part of war reparations, and sometimes was accompanied by the valuable tacit knowledge of technical experts. E.W. Kutzscher, for example, was flown to Britain from Kiel after the war, and subsequently had an important influence on American developments when he joined Lockheed Aircraft Co. in Burbank, California as a research scientist.

Although the fabrication methods developed for lead salt photoconductors was usually not completely understood, their properties are well established and reproducibility could only be achieved after following well-tried recipes. Unlike most other semiconductor IR detectors, lead salt photoconductive materials are used in the form of polycrystalline films approximately 1 μm thick and with individual crystallites ranging in size from approximately 0.1–1.0 μm. They are usually prepared by chemical deposition using empirical recipes, which generally yields better uniformity of response and more stable results than the evaporative methods. In order to obtain high-performance detectors, lead chalcogenide films need to be sensitized by oxidation. The oxidation may be carried out by using additives in the deposition bath, by post-deposition heat treatment in the presence of oxygen, or by chemical oxidation of the film. The effect of the oxidant is to introduce sensitizing centres and additional states into the bandgap and thereby increase the lifetime of the photoexcited holes in the p-type material.

3. Classification of infrared detectors

Observing a history of the development of the IR detector technology after World War II, many materials have been investigated. A simple theorem, after Norton [40], can be stated: "All physical phenomena in the range of about 0.1–1 eV will be proposed for IR detectors". Among these effects are: thermoelectric power (thermocouples), change in electrical conductivity (bolometers), gas expansion (Golay cell), pyroelectricity (pyroelectric detectors), photon drag, Josephson effect (Josephson junctions, SQUIDs), internal emission (PtSi Schottky barriers), fundamental absorption (intrinsic photodetectors), impurity absorption (extrinsic photodetectors), low dimensional solids [superlattice (SL), quantum well (QW) and quantum dot (QD) detectors], different type of phase transitions, etc.

Figure 6 gives approximate dates of significant development efforts for the materials mentioned. The years during World War II saw the origins of modern IR detector technology. Recent success in applying infrared technology to remote sensing problems has been made possible by the successful development of high-performance infrared detectors over the last six decades. Photon IR technology combined with semiconductor material science, photolithography technology developed for integrated circuits, and the impetus of Cold War military preparedness have propelled extraordinary advances in IR capabilities within a short time period during the last century [41].

The majority of optical detectors can be classified in two broad categories: photon detectors (also called quantum detectors) and thermal detectors.

3.1. Photon detectors

In photon detectors the radiation is absorbed within the material by interaction with electrons either bound to lattice atoms or to impurity atoms or with free electrons. The observed electrical output signal results from the changed electronic energy distribution. The photon detectors show a selective wavelength dependence of response per unit incident radiation power (see Fig. 8). They exhibit both a good signal-to-noise performance and a very fast response. But to achieve this, the photon IR detectors require cryogenic cooling. This is necessary to prevent the thermal

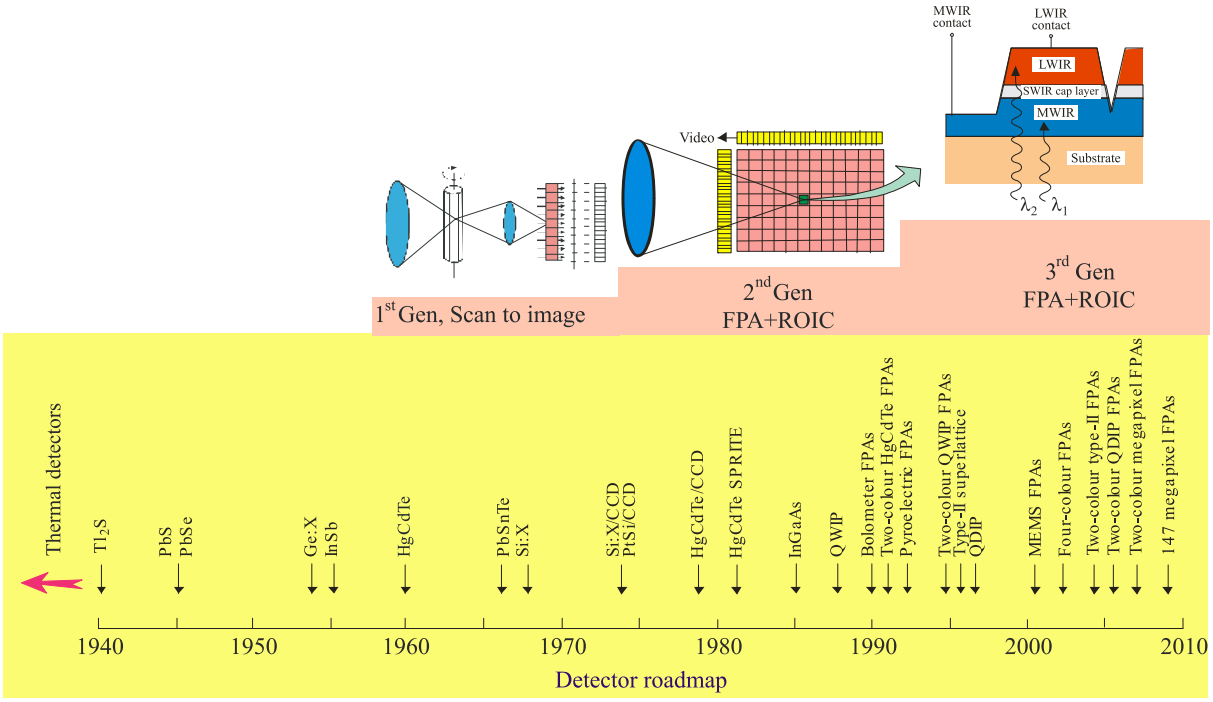

Fig. 6. History of the development of infrared detectors and systems. Three generation systems can be considered for principal military and civilian applications: 1st Gen (scanning systems), 2nd Gen (staring systems – electronically scanned) and 3rd Gen (multicolour functionality and other on-chip functions).

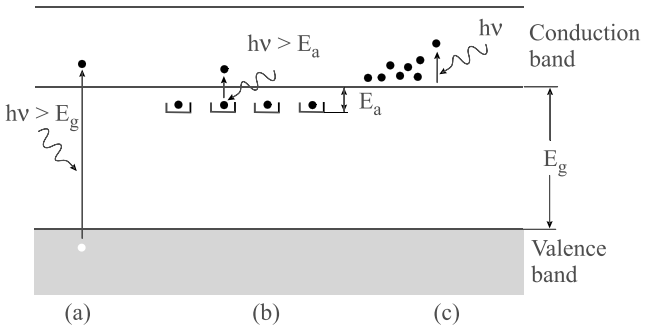

Fig. 7. Fundamental optical excitation processes in semiconductors: (a) intrinsic absorption, (b) extrinsic absorption, (c) free carrier absorption.

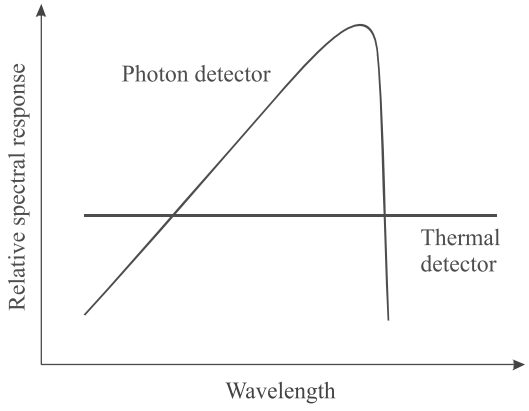

Fig. 8. Relative spectral response for a photon and thermal detector.

generation of charge carriers. The thermal transitions compete with the optical ones, making non-cooled devices very noisy.

The spectral current responsivity of photon detectors is equal to

$$R_i = \frac{\lambda \eta}{hc} qg\,, \tag{1}$$

where λ is the wavelength, h is the Planck's constant, c is the velocity of light, q is the electron charge, and g is the photoelectric current gain. The current that flows through the contacts of the device is noisy due to the statistical nature of the generation and recombination processes – fluctuation of optical generation, thermal generation, and radiative and nonradiative recombination rates. Assuming that the current gain for the photocurrent and the noise current are the same, the noise current is

$$I_n^2 = 2q^2 g^2 (G_{op} + G_{th} + R)\Delta f, \tag{2}$$

where G_{op} is the optical generation rate, G_{th} is the thermal generation rate, R is the resulting recombination rate, and Δf is the frequency band.

It was found by Jones [42], that for many detectors the noise equivalent power (*NEP*) is proportional to the square root of the detector signal that is proportional to the detector area, A_d. The normalized detectivity D^* (or D-star) suggested by Jones is defined as

$$D^* = \frac{(A_d)^{1/2}}{NEP}. \tag{3}$$

Detectivity, D^*, is the main parameter to characterize normalized signal-to-noise performance of detectors and can be also defined as

$$D^* = \frac{R_i (A_d \Delta f)^{1/2}}{I_n}. \tag{4}$$

The importance of D^* is that this figure of merit permits comparison of detectors of the same type, but having different areas. Either a spectral or blackbody D^* can be defined in terms of corresponding type of *NEP*.

At equilibrium, the generation and recombination rates are equal. In this case

$$D^* = \frac{\lambda \eta}{2hc(Gt)^{1/2}}. \tag{5}$$

Background radiation frequently is the main source of noise in a IR detector. Assuming no contribution due to recombination,

$$I_n^2 = 2\Phi_B A_d \eta q^2 g^2 \Delta f, \tag{6}$$

where Φ_B is the background photon flux density. Therefore, at the background limited performance conditions (BLIP performance)

$$D^*_{BLIP} = \frac{\lambda}{hc}\left(\frac{\eta}{\Phi_B}\right)^{1/2}. \tag{7}$$

Once background-limited performance is reached, quantum efficiency, η, is the only detector parameter that can influence a detector's performance.

Depending on the nature of the interaction, the class of photon detectors is further sub-divided into different types. The most important are: intrinsic detectors, extrinsic detectors, photoemissive (Schottky barriers). Different types of detectors are described in details in monograph *Infrared Detectors* [41]. Figure 9 shows spectral detectivity curves for a number of commercially available IR detectors.

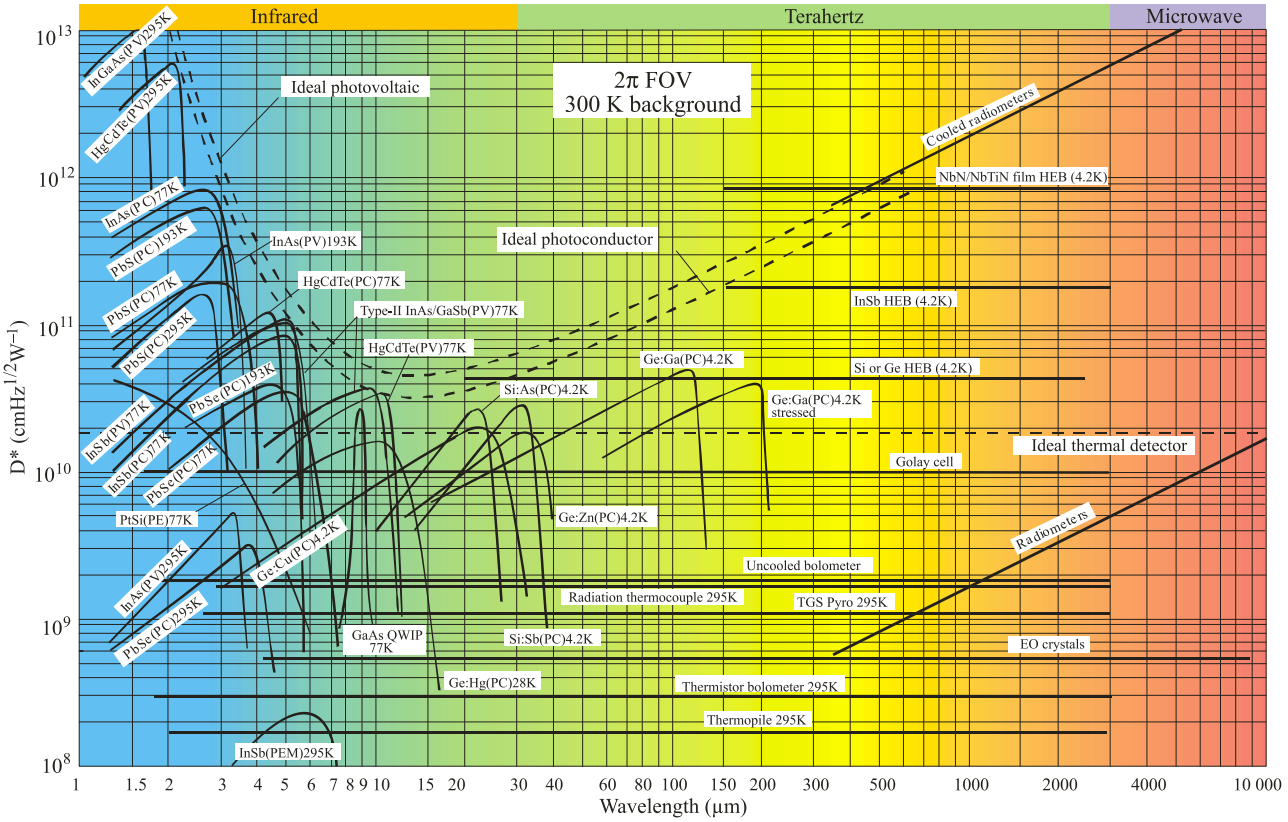

Fig. 9. Comparison of the D^* of various available detectors when operated at the indicated temperature. Chopping frequency is 1000 Hz for all detectors except the thermopile (10 Hz), thermocouple (10 Hz), thermistor bolometer (10 Hz), Golay cell (10 Hz) and pyroelectric detector (10 Hz). Each detector is assumed to view a hemispherical surrounding at a temperature of 300 K. Theoretical curves for the background-limited D^* (dashed lines) for ideal photovoltaic and photoconductive detectors and thermal detectors are also shown. PC – photoconductive detector, PV – photovoltaic detector, PEM – photoelectromagnetic detector, and HEB – hot electron bolometer.

BLIP

Background-Limited Infrared Photodetection

The total generation rate is a sum of the optical and thermal generation

$$G = G_{\text{th}} + G_{\text{op}}. \tag{10'}$$

The optical generation may be due to the signal or background radiation. For infrared detectors, usually background radiation is higher compared to the signal radiation. If the thermal generation is reduced much below the background level, the performance of the device is determined by the background radiation (BLIP conditions for Background Limited Infrared Photodetector). This condition can be described as

$$\frac{\eta \Phi_{\text{B}} \tau}{t} > n_{\text{th}}, \tag{11}$$

where n_{th} is the density of thermal carriers at the temperature T, and τ is the carrier lifetime, and Φ_{B} is the total background photon flux density (unit $\text{cm}^{-2}\,\text{s}^{-1}$) reaching the detector. Re-arranging we have for the BLIP requirements

$$G_{\text{op}} = \frac{\eta \Phi_{\text{B}}}{t} > \frac{n_{\text{th}}}{\tau} = G_{\text{th}}, \tag{12}$$

i.e. the photon generation rate per unit volume needs to be greater than the thermal generation rate per unit volume. The carriers can be either majority or minority in nature.

7.1. FPA architectures

Two families of multielement detectors can be considered; one used for scanning systems and the other used for staring systems. The simplest scanning linear FPA consists of a row of detectors [Fig. 13(a)]. An image is generated by scanning the scene across the strip using, as a rule, a mechanical scanner. At standard video frame rates, at each pixel (detector) a short integration time has been applied and the total charges are accommodated. A staring array is a 2-D array of detector pixels [Fig. 4(b)] which are scanned electronically. These types of arrays can provide enhanced sensitivity and gain in camera weight.

The scanning system, which does not include multiplexing functions in the focal plane, belongs to the first generation systems. A typical example of this kind of detector is a linear photoconductive array (PbS, PbSe, HgCdTe) in which an electrical contact for each element of a multielement array is brought off the cryogenically-cooled focal plane to the outside, where there is one electronic channel at ambient temperature for each detector element. The US common module HgCdTe arrays employ 60, 120 or 180 photoconductive elements depending on the application.

The second generation systems (full-framing systems), which are at present being developed, have at least three orders of magnitude more elements ($>10^6$) on the focal plane than first generation systems and the detectors elements are configured in a 2-D array. These staring arrays are scanned electronically by circuits integrated

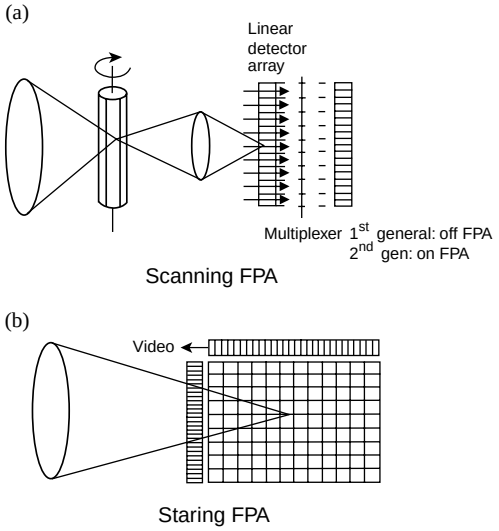

Fig. 13. (a) Scanning focal plane array and (b) staring focal plane array.

with the arrays. These readout integrated circuits (ROICs) include, e.g., pixel deselecting, antiblooming on each pixel, subframe imaging, output preamplifiers, and some other functions.

Intermediary systems are also fabricated with multiplexed scanned photodetector linear arrays in use and with, as a rule, time delay and integration (TDI) functions. Typical examples of these systems are HgCdTe multilinear 288×4 arrays fabricated by Sofradir both for 3–5-μm and 8–10.5-μm bands with signal processing in the focal plane (photocurrent integration, skimming, partitioning, TDI function, output preamplification and some others).

A number of architectures are used in the development of IR FPAs [40]. In general, they may be classified as hybrid and monolithic, but these distinctions are often not as important as proponents and critics state them to be. The central design questions involve performance advantages versus ultimate producibility. Each application may favour a different approach depending on the technical requirements, projected costs and schedule.

Hybrid FPAs detectors and multiplexers are fabricated on different substrates and mated with each other by flip-chip bonding or loophole interconnection (Fig. 14). First demonstration in the mid-1970s, indium bump bonding of readout electronics provides for multiplexing the signals from thousands pixels onto a few output lines, greatly simplifying the interface between the vacuum-enclosed cryogenic sensor and the system electronics. Two hybridization approaches are in use today. In one approach, indium bumps are formed on both the detector array and the ROIC chip. The array and the ROIC are aligned and force is applied to cause the indium bumps to cold-weld together. In the other approach, indium bumps are formed only on the ROIC; the detector array is brought into alignment and proximity with the ROIC, the temperature is raised to cause the indium to melt, and contact is made by reflow. Today, millions of pixels are connected to millions of amplifiers/integrators in the unit cells of readout circuits. In this case we can optimise the detector material and multiplexer independently. Other advantages of the hybrid FPAs are near 100% fill factors and increased signal-processing area on the multiplexer chip.

The detector array can be illuminated from either the frontside (with the photons passing through the transparent silicon multiplexer) or backside (with photons passing through the transparent detector array substrate). In general, the latter approach is most advantageous, as the multiplexer will typically have areas of metallizations and other opaque regions, which can reduce the effective optical area of the structure. In HgCdTe hybrid FPAs, photovoltaic detectors are formed on thin HgCdTe epitaxial layers on transparent CdTe or CdZnTe substrates. For HgCdTe flip-chip hybrid technology, the maximum chip size is of the order of 10-mm^2. To overcome this problem, PACE (producible alternative to CdTe for epitaxy) technology is being developed with sapphire or silicon as the substrate of HgCdTe detectors. A SWIR 1024×1024 element HgCdTe hybrid FPA was developed using the PACE technology [41]. When using opaque materials, substrates must be thinned to 10–20 μm to obtain sufficient quantum efficiencies and reduce crosstalk. In the "indirect" backside illuminated configuration both the detector array and the silicon ROIC chip are bump mounted side-by-side onto a common circuit board. The

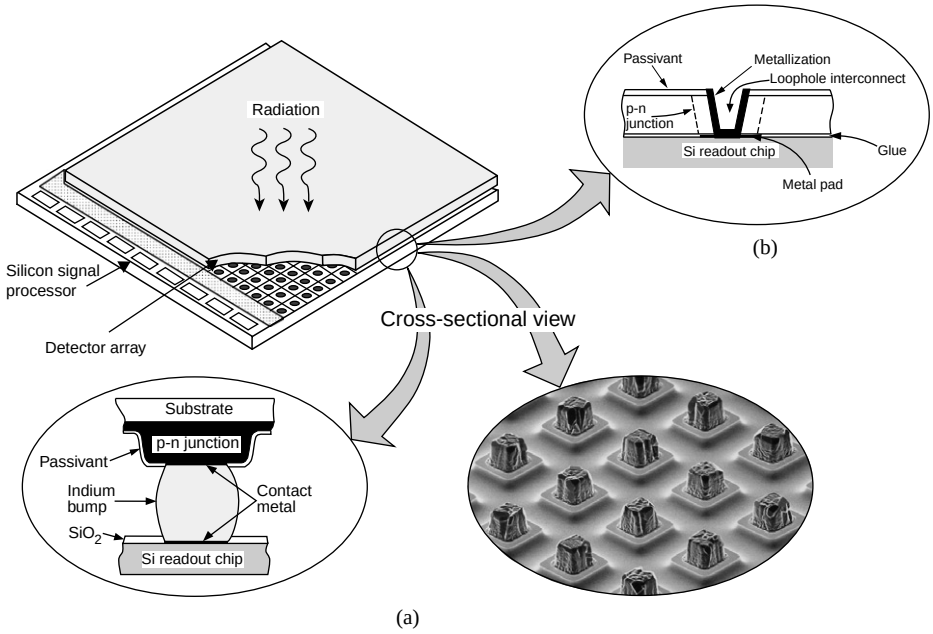

Fig. 14. Hybrid IR FPA with independently optimised signal detection and readout: (a) indium bump technique, (b) loophole technique.

"indirect" configuration allows the unit cell area in the silicon ROIC to be larger than the detector area and is usually used for small scanning FPAs, where stray capacitance is not an issue.

In the loophole interconnection, the detector and the multiplexer chips are glued together to form a single chip before detector fabrication [42]. The photovoltaic detector is formed by ion implantation and loopholes are drilled by ion-milling and electrical interconnection between each detector and its corresponding input circuit is made through a small hole formed in each detector. The junctions are connected down to the silicon circuit by cutting the fine, few μm in diameter holes through the junctions by ion milling, and then backfilling the holes with metallization. The thermal expansion mismatch problem is approached by using about 10-μm thick p-type HgCdTe, bonded rigidly to the silicon so that strain is taken up elastically. This makes the devices mechanically and electrically very robust with contact obscuration typically less than 10%. The disadvantages include the necessity of mechanical thinning of the HgCdTe, which may lead to damage that may affect photodiode performance and the necessity of devising clever low-temperature techniques for junction formation and passivation because of the presence of the epoxy (e.g., the ion milling process to form the *n*-type regions is done at room temperature). A similar type of hybrid technology called VIMS (vertically integrated metal–insulator–semiconductor) was reported by DRS Infrared Technologies (former Texas Instruments).

8. Photon detectors

The increased sensitivity, resolution in system complexity of FPAs offer significant advantages in military as well as civilian applications in thermal imaging, guidance, reconnaissance, surveillance, ranging and communication systems. From fundamental considerations HgCdTe is the most important semiconductor alloy system for IR detectors in the spectral range between 1 and 25 μm. HgCdTe detectors as the intrinsic photon detectors absorb the IR radiation across the fundamental energy gap and are characterized by high optical absorption coefficient and quantum efficiency and relatively low thermal generation rate compared to extrinsic detectors, silicide Schottky barriers and QWIPs. The operating temperature for intrinsic detectors is, therefore, higher than for other types of photon detectors. The attributes of HgCdTe translate to flexibility and the capability to produce short wavelength infrared (SWIR), MWIR and LWIR detectors. HgCdTe has, however, serious technological problems in mass production, which result from a weak Hg–Te bond. The basic problems are: health hazard due to the highly toxic compounds, high mercury vapour pressure over melts, the Hg–Cd–Te phase diagram shape resulting in serious difficulties in repeatable growth of uniform-composition bulk crystals and epitaxial layers. Uniformity and yield are still issues. The majority of these problems

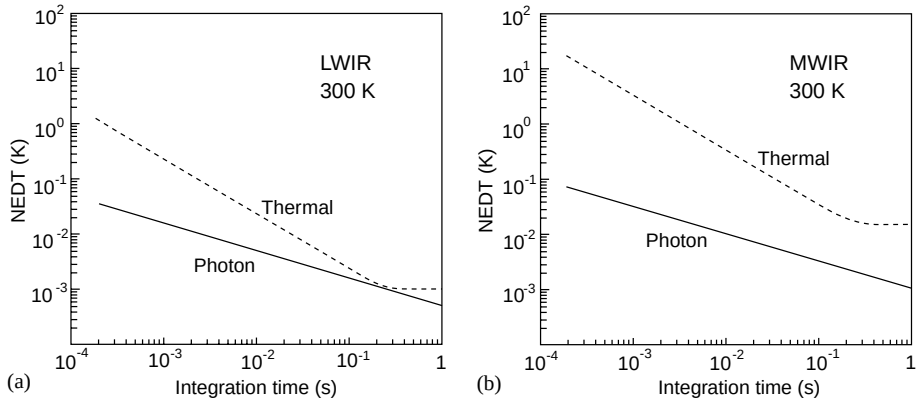

Fig. 24. Theoretical NEDT comparison of uncooled thermal and HgCdTe uncooled photon LWIR (a) and MWIR (b) detectors (after Ref. [56]).

have been successfully overcome. However, in spite of the achievements in material and device quality, difficulties still exist due to lattice, surface, and interface instabilities, which can lead to large variation in stoichiometry and transport properties as a result of treatments as diverse as oxidation, mechanical damage, and reaction with metals. The difficulties with this material have made it desirable to examine other material systems to determine whether performance can be improved. However,

- None of the new materials offers fundamental advantages over HgCdTe.

- HgCdTe exhibits extreme flexibility, it can be tailored for optimised detection at any region of IR spectrum, dual and multicolour devices can be easily constructed.
- Present development of IR photodetectors has been dominated by complex band gap heterostructures. Among various variable band gap semiconductor alloys, HgCdTe is the only material covering the whole IR spectral range having nearly the same lattice parameter. The difference of lattice parameter between CdTe ($E_g = 1.5\,eV$) and $Hg_{0.8}Cd_{0.2}Te$ ($E_g = 0.1\,eV$) is $\approx 0.2\%$ (see Fig. 25). Replacing small fraction of Cd with Zn or Te with Se can compensate the residual lattice mismatch. The independence of lattice parameter on composition is a major advantage of HgCdTe over any other materials.

Epitaxy is the preferable technique to obtain device-quality materials. Among the various epitaxial techniques, liquid phase epitaxy (LPE) is the most mature method for production of both first- and second-generation tactical detectors. LPE growth must be carried out at relatively high growth temperature with adherent interdiffusion and resulting graded interfaces. Recent efforts are aimed mostly at low growth temperature techniques: metalorganic chemical vapour deposition

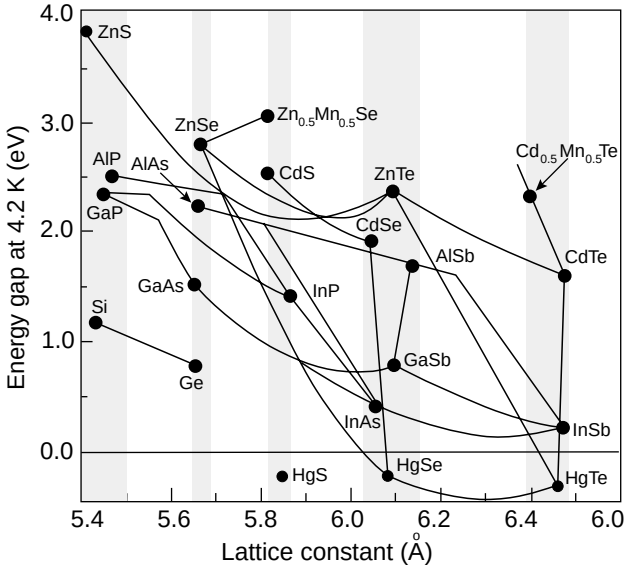

Fig. 25. A plot of the low temperature energy bandgaps of a number of semiconductors with the diamond and zinc-blende structure versus their lattice constants. The shaded regions highlight several families of semiconductors with similar lattice constants. $Cd_{0.96}Zn_{0.04}Te$ is a good match for a wide range of MWIR to LWIR HgCdTe alloys.

(MOCVD) and molecular beam epitaxy (MBE). At this time, MBE has become the dominant vapour-phase growth method for HgCdTe. Although the quality of MBE material is not yet on a par with LPE, it made tremendous progress in the past decade to the point where a variety of high-background device formats have been successfully demonstrated using this growth technique. Key to this success was ability to dope layers, both p- and n-type, and reduction of etch pit densities to below $10^7/cm^2$.

8.1. HgCdTe photodiodes

Different HgCdTe photodiode architectures have been fabricated that are compatible with backside and frontside illuminated hybrid FPA technology. Cross section views of these various architectures are shown in Figs. 26 and 27. The most important architectures are also included in Table 4, which summarises the applications of HgCdTe photodiode designs by the major FPA manufactures today.

Table 4 contains description of representative HgCdTe FPAs that are commercially available and described on web sides of the major HgCdTe manufactures. The LWIR FPAs usually operate at 77 K and are near the BLIP limit for higher background fluxes. The MWIR FPAs operate at temperatures above 77 K, and they are often thermoelectrically cooled. Their temperature operation depends on the design of the ROIC. Standard products for SWIR may be operated

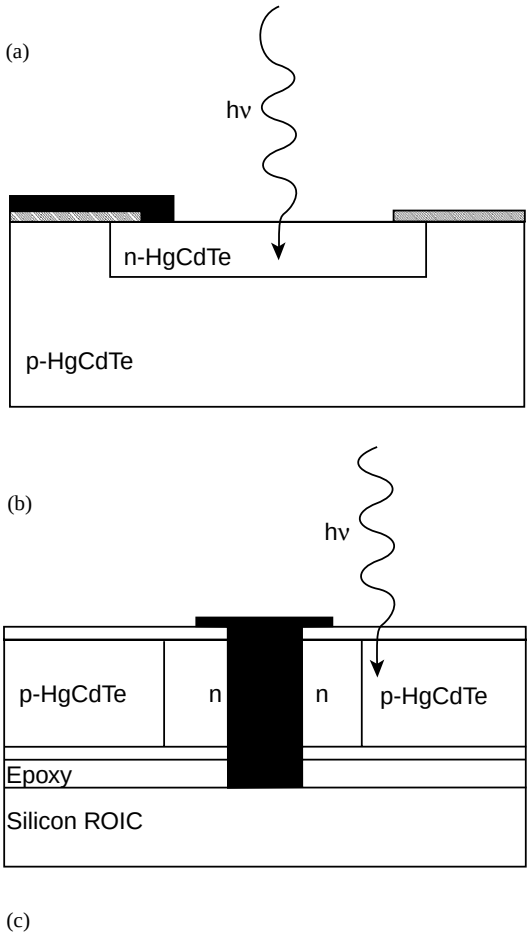

double-ionized Hg vacancy

IMPORTANT:

As-grown undoped $x_{Cd} \sim 0.2$ material is invariably p-type at 77 K due to V''_{Hg} incorporated during growth under Te-rich conditions. CTC is achieved by reducing $[V''_{Hg}]$ to below the background residual donor level by thermal annealing under Hg saturation. The removal of V''_{Hg} is due to the capture of fast in-diffusing metal interstitials and to the slower out-diffusion of V''_{Hg}. (CTC means: "Conductivity Type Conversion")

Fig. 26. Frontside illuminated HgCdTe photodiode architectures: (a) planar Hg-diffused n-on-p homojunction, (b) n–p "loophole" homojunction

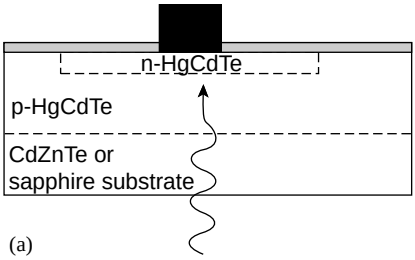

(a)

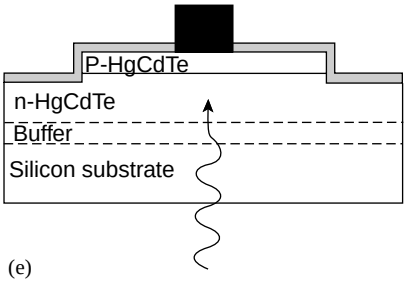

(e)

Fig. 27. Backside illuminated HgCdTe photodiode architectures: (a) planar ion implanted n^+–n^-–p homojunction, (e) backside illuminated mesa P-on-n heterojunction on silicon substrate

at room temperature. Table 4 does not contain complete list of products, but it illustrates the range of HgCdTe FPAs wavelengths, formats, unit cell size, and describes the FPA performance (D^* and NEDT) that can be considered as commercially available.

8.1.1. Frontside illuminated photodiodes

The frontside illuminated n-on-p homojunction [see Fig. 26(a)] was the first HgCdTe device structure pioneered by Societe Anonyme de Telecommunications (SAT) [62]. Hg in-diffusion into vacancy doped HgCdTe has been the most widely used for very fast photodiodes [63]. Hg is diffused through openings formed in an

Table 4
HgCdTe photodiode architectures used for hybrid FPAs (after Ref. [61])

Configuration	Junction formation	Company
n-on-p VIP	Ion implantation forms n-on-p diode in p-type HgCdTe, grown by Te-solution LPE on CdZnTe and epoxied to silicon ROIC wafer; over the edge contact	DRS infrared technologies (formerly Texas Instruments)
n–p loophole	Ion beam milling forms n-type islands in p-type Hg-vacancy-doped layer grown by Te-solution LPE on CdZnTe, and epoxied onto silicon ROIC wafer; cylindrical lateral collection diodes	BAE Systems Ltd (formerly GEC-Marconi Infrared (GMIRL))
n^+-on-p planar	Ion implant into acceptor-doped p-type LPE film grown by Te-solution slider	Sofradir (Societe Francaise de Detecteurs Infrarouge)
n^+–n^-–p planar homojunctions	Boron implant into Hg-vacancy p-type, grown by Hg-solution tipper on 3" dia. sapphire with MOCVD CdTe buffer; ZnS passivation	Rockwell/Boeing
P-on-n mesa	1. Two-layer LPE on CdZnTe: Base: Te-solution slider, indium-doped Cap: Hg-solution dipper, arsenic-doped 2. MOCVD in situ on CdZnTe Iodine-doped base, arsenic-doped cap	IR Imaging Systems, Sanders—A Lockheed Martin Company (LMIRIS)
P-on-n mesa	1. Two-layer LPE on CdZnTe or Si: Base: Hg-solution dipper, indium-doped Cap: Hg-solution dipper, arsenic-doped 2. MBE in situ on CdZnTe or Si Indium-doped base, arsenic-doped cap	Raytheon Infrared Center of Excellence (RIRCoE, formerly SBRC) and Hughes Research Laboratories (HRLs)
P-on-n planar buried heterostructure	Arsenic implant into indium-doped N–n or N–n–N film grown by MBE on CdZnTe	Rockwell/Boeing

insulator layer, lowering the Hg vacancy concentration below that of the donors, which are either intentionally introduced dopants or residual impurities. For this device structures, the first use of an interdiffused CdTe layer for heterostructure passivation was reported [64].

Conversion of vacancy doped p-type HgCdTe to n-type during low-energy ion milling became another important technique of junction fabrication [see Fig. 26(b)]. GEC-Marconi Infrared Laboratories uses 25–30-μm thick LPE layer (grown from Te-rich solution) epoxied to a silicon CMOS ROIC [65]. A small hole, 5-μm in diameter, is created by ion milling. Just as in the case of ion implanted n-on-p junction, the n-type region is formed when Hg atoms are liberated during the milling process. The Hg atoms diffuse laterally, annihilating Hg vacancy acceptors and uncovering residual and intentional donors. The detector processing incorporates a metalization of small holes which connect one side of the junction to the input circuit node directly beneath. In this device geometry, photocarriers are collected by lateral diffusion.

8.1.2. Backside illuminated photodiodes

The first architecture used for hybrid HgCdTe FPAs was backside illuminated planar ion implanted n^+–n^-–p homojunction [see Fig. 27(a)]. The based p-type absorber layer was grown by LPE onto an IR-transparent substrate such as CdTe, CdZnTe or sapphire. During implantation process, interstitial Hg atoms are liberated, diffused inward, annihilating Hg vacancies and forming an n^--region beneath the n^+-implanted layer [67]. In non-doped HgCdTe, the acceptors are the Hg vacancies and short lifetime in p-type region values are observed.

The last HgCdTe photodiode architecture shown in Fig. 27(e) can be fabricated using silicon substrates.

CHAPTER **2**

Quantum Well Infrared Photodetectors

S. D. Gunapala, S. V. Bandara, S. B. Rafol, and
* **D. Z. Ting**

Contents

* Center for Infrared Sensors, Jet Propulsion Laboratory, California Institute of Technology, Pasadena, CA 91109, USA

Semiconductors and Semimetals, Volume 84
ISSN 0080-8784, DOI: 10.1016/B978-0-12-381337-4.00002-4

1. INTRODUCTION

Intrinsic infrared detectors in the mid-wavelength and long-wavelength ranges are based on interband transition, which promotes an electron across the band gap (E_g) from the valence band to the conduction band as shown in Fig. 2.1. These photoexcited-electrons can be collected efficiently, thereby producing a photocurrent in the external circuit. Because the incoming photon has to excite an electron from the valence band to the conduction band, the energy of the photon ($h\nu$) must be higher than the band gap of the photosensitive material. One possible way of detecting the infrared radiation is using narrow band-gap semiconductors such as HgCdTe and InSb, which is described in the previous chapter of this volume. The other possibility is to create artificial, narrow band gaps by high band-gap materials such as GaAs. The second method involves multi-quantum-wells (MQWs) and superlattices structures. This chapter

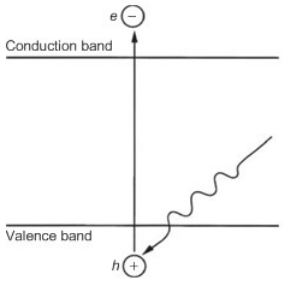

FIGURE 2.1 Band diagram of conventional intrinsic infrared photodetector. (Gunapala and Bandara, 1995)

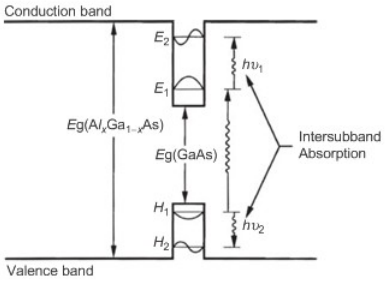

FIGURE 2.2 Schematic band diagram of a quantum well. Intersubband absorption can take place between the energy levels of a quantum well associated with the conduction band (n-doped) or the valence band (p-doped). (Levine, 1993)

describes the use of MQW-based intersubband transition for infrared detection (Fig. 2.2). Additionally, the spectral response of the detectors can be tuned by controlling the E_g of the photosensitive material.

The idea of using MQW structures to detect infrared radiation can be explained by using the basic principles of quantum mechanics. The quantum well is equivalent to the well-known "particle in a box" problem in quantum mechanics, which can be solved by the time independent Schrodinger equation. The solutions to this problem are the Eigen values that describe energy levels inside the quantum well in which the particle is allowed to exist. The positions of the energy levels are primarily determined by the quantum-well dimensions (height and width). For the infinitely-high barriers and parabolic bands, the energy levels in the quantum well are given by Weisbuch (1987)

$$E_j = \left(\frac{\hbar^2\pi^2}{2m^*L_w^2}\right)j^2, \tag{2.1}$$

where L_w is the width of the quantum well, m^* is the effective mass of the carrier in the quantum well, and j is an integer. Thus, the intersubband energy between the ground and the first excited state is

$$(E_2 - E_1) = (3\hbar^2\pi^2/2m^*L_w^2). \tag{2.2}$$

The quantum-well infrared photodetectors (QWIPs) discussed in this article use the photo-excitation of the electron (hole) between the ground

state and the first excited state in the conduction band (valance band) quantum well (See Fig. 2.2). The quantum-well structure is designed so that these photoexcited carriers can escape from the quantum well and get collected as photocurrent. In addition to the larger intersubband oscillator strength, these detectors afford greater flexibility than the extrinsically doped semiconductor infrared detectors because the wavelength of the peak response and the cutoff can be continuously tailored by varying the layer thickness (quantum-well width) and the barrier composition (barrier height).

The lattice-matched GaAs/$Al_xGa_{1-x}As$ material system is a very good candidate to create such a quantum-well structure, because the band gap of $Al_xGa_{1-x}As$ can be changed continuously by varying the x value (and hence the height of the quantum well). Thus, by changing the quantum-well width L_w and the barrier height (Al molar ratio of $Al_xGa_{1-x}As$ alloy), this intersubband transition energy can be varied over a wide range, from short-wavelength infrared (SWIR; 1–3 μm), mid wavelength-infrared (MWIR; 3–5 μm), through long-wavelength (LWIR; 8–12 μm), and into the VLWIR (>12 μm). It is important to note that unlike intrinsic detectors, which utilize interband transition, quantum wells of these detectors must be doped because the photon energy is not sufficient to create photocarriers ($h\nu < E_g$).

The possibility of using GaAs/$Al_xGa_{1-x}As$ MQW structures to detect infrared radiation was first suggested by Esaki and Sakaki (1977), experimentally investigated by Smith *et al.* (1983), and theoretically analyzed by Coon and Karunasiri (1984). The first experimental observation of the strong intersubband absorption was performed by West and Eglash (1985), and the first QWIP was demonstrated by Levine *et al.* (1987b) at Bell Laboratories. Levine *et al.* (1988c) also introduced QWIP involving bound-to-continuum intersubband transitions with wider $Al_xGa_{1-x}As$ barriers and demonstrated dramatically-improved detectivity. Recent developments in these detectors have already led to the demonstration of large, high-sensitivity staring arrays by several groups (Andersson *et al.*, 1997; Breiter *et al.*, 1998; Choi *et al.*, 2009; Goldberg *et al.*, 2005; Gunapala *et al.*, 2005a, 2010, 2003a; Rafol 2008b; Rafol and Cho 2008a; Rafol *et al.*, 2007; Robo *et al.*, 2009; Schneider *et al.*, 2004).

2. COMPARISON OF VARIOUS TYPES OF QWIPS

2.1. n-Doped QWIPs

As mentioned previously, the first *bound-to-bound* state QWIP was demonstrated by Levine *et al.* (1987b). It consisted of 50 periods of $L_w = 65$ Å GaAs

and $L_b = 95$ Å $Al_{0.25}Ga_{0.75}As$ barriers sandwiched between the top (0.5 μm thick) and the bottom (1 μm thick) GaAs contact layers. The center 50 Å of the GaAs wells were doped to $N_D = 1.4 \times 10^{18}\,cm^{-3}$ and the contact layers were doped to $N_D = 4 \times 10^{18}\,cm^{-3}$. This structure was grown by the molecular beam epitaxy (MBE). These thicknesses and compositions were chosen to produce only two states in the quantum well with energy spacing giving rise to a peak wavelength of 10 μm. The measured (Levine *et al.*, 1987b) absorption spectra peaked at $\lambda_p = 10.9\,\mu m$ with a full-width at half-maximum of $\Delta\upsilon = 97\,cm^{-1}$. The peak absorbance $a = -\log(\text{transmission}) = 2.2 \times 10^{-2}$ corresponds to a net absorption of 5% (i.e., $a = 600\,cm^{-1}$).

After the absorption of infrared photons, the photoexcited carriers can be transported either along the plane of quantum wells (with an electric field along the quantum wells) or perpendicular to the wells (with an electric field perpendicular to the epitaxial layers). As far as the infrared detection is concerned, perpendicular transport is superior to parallel transport (Wheeler and Goldberg, 1975) because the difference between the excited state and the ground state mobilities is much larger in the latter case, and consequently, transport perpendicular to the quantum wells (i.e., growth direction) gives a substantially-high photocurrent. In addition, the heterobarriers block the transport of ground-state carriers in the quantum wells, and thus the lower-dark current. For these reasons, QWIPs are based on the escape and perpendicular transport of photoexcited carriers as shown in Fig. 2.3.

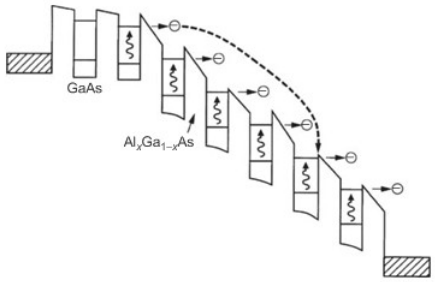

FIGURE 2.3 Conduction-band diagram for a bound-to-bound QWIP, showing the photoexcitation (intersubband transition) and tunneling out of well. (Levine, 1993)

In the later versions of the bound-to-bound state QWIPs, Choi *et al.* (1987c) has used slightly thicker and higher barriers to reduce the tunneling-induced dark current. When they increased the barrier thickness from $L_b = 95$ Å to 140 Å and $Al_xGa_{1-x}As$ barrier height from $x = 0.25$ to 0.36, the dark current (also the photocurrent) was significantly reduced. The nonlinear behavior of the responsivity and the dark current versus bias voltage observed in the bound-to-bound QWIPs are due to the complex tunneling process associated with the high-field domain formation (Choi *et al.*, 1987c).

2.3. n-Doped Bound-to-Continuum QWIPs

In the previous section, we mentioned the QWIP containing two bound states. By reducing the quantum well width, it is possible to push the strong bound-to-bound intersubband absorption into the continuum, resulting in a strong bound-to-continuum intersubband absorption. The major advantage of the bound-to-continuum QWIP is that the photoexcited electron can escape from the quantum well to the continuum transport states without tunneling through the barrier as shown in Fig. 2.4. As a result, the bias required to efficiently collect the photoelectrons can be reduced dramatically, and hence lower the dark current. Due to the fact that the photoelectrons do not have to tunnel through the barriers, the $Al_xGa_{1-x}As$ barrier-thickness of the bound-to-continuum QWIP can be increased without reducing the photoelectron collection efficiency. Increasing the barrier width from a few hundred Å to 500 Å can reduce the ground-state sequential tunneling by an order of magnitude. By making use of these improvements, Levine *et al.* (1990a) has successfully demonstrated the first bound-to-continuum QWIP with a dramatic improvement

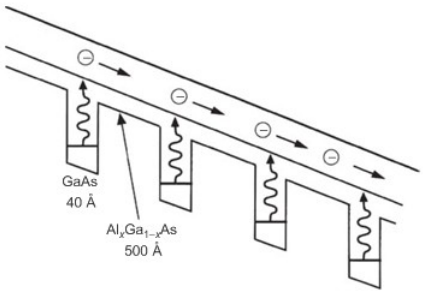

FIGURE 2.4 Conduction-band diagram for a bound-to-continuum QWIP, showing the photoexcitation and hot-electron transport process. (Levine, 1993)

in the performance (i.e., detectivity 3×10^{10} cm$\sqrt{\text{Hz}}$/W at 68 K for a QWIP which had cutoff wavelength at 10 μm).

2.4. n-Doped Bound-to-Quasibound QWIPs

Improving the QWIP performance depends largely on minimizing the parasitic current (i.e., dark current) that plagues all the light detectors. The dark current is the current that flows through a biased detector in the dark (i.e., with no photons impinging on it). As Gunapala and Bandara (1995) have discussed elsewhere, at temperatures above 45 K (typical for $\lambda < 14\,\mu$m), the dark current of the QWIP is entirely dominated by the classical thermionic emission of the ground-state electrons directly out of the well into the energy continuum. Minimizing the dark current is critical to the commercial success of the QWIP as it allows the highly-desirable high-temperature detector operation.

Therefore, Gunapala and Bandara (1995) have designed the *bound-to-quasibound* quantum well by placing the first excited state exactly at the well top as shown in Fig. 2.5. The best previous QWIPs pioneered by Levine *et al.* (1988c) at AT&T Bell Laboratories were of the bound-to-continuum variety, so-called because the first excited state was a continuum energy band above the quantum well top (typically 10 meV). Dropping the first excited state to the quantum well-top causes the barrier to thermionic emission (roughly the energy height from the ground state to the well top) to be ~10 meV more in the bound-to-quasibound

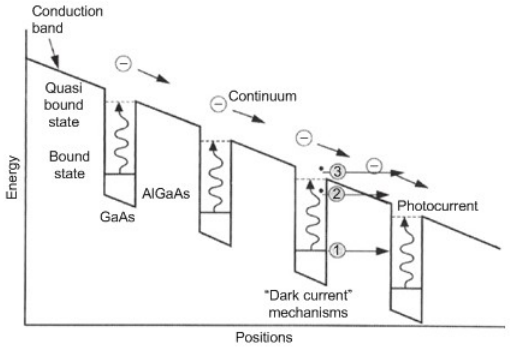

FIGURE 2.5 Schematic diagram of the conduction band in a bound-to-quasibound QWIP in an externally applied electric field. Absorption of infrared photons can photoexcite electrons from the ground state of the quantum well into the continuum, causing a photocurrent. Three dark current mechanisms are also shown: ground state tunneling (1); thermally assisted tunneling (2); and thermionic emission.

QWIP than in the bound-to-continuum one, causing the dark current to drop significantly at the elevated operating temperatures. The advantage of the bound-to-quasibound QWIP over the bound-to-continuum QWIP is that in the case of bound-to-quasibound QWIP, the energy barrier for the thermionic emission is same as it is for the photoionization as shown in Fig. 2.5 (Gunapala and Bandara, 1995). In the case of a bound-to-continuum QWIP, the energy barrier for the thermionic emission is 10–15 meV less than the photoionization energy. Thus, the dark current of the bound-to-quasibound QWIPs is reduced by an order of magnitude (i.e., $I_d \propto e^{-\frac{\Delta E}{kT}} \approx e^{-2}$ for $T = 55$ K) as shown in Fig. 2.5.

2.5. n-Doped Broadband QWIPs

A broad-band MQW structure can be designed by repeating a unit of several quantum wells with slightly different parameters such as quantum-well width and barrier height. The first device structure (shown in Fig. 2.6) demonstrated by Bandara *et al.* (1998a) has 33 repeated layers of GaAs and three-quantum-well units separated by $L_B \sim 575$ Å thick $Al_xGa_{1-x}As$ barriers (Bandara *et al.*, 1998b). The well thicknesses of the quantum

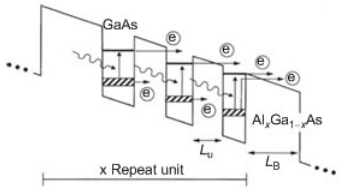

FIGURE 2.6 Schematic diagram of the conduction band in broadband QWIP in an externally applied electric field. The device structure consists of 33 repeated layers of three-quantum-well units separated by thick $Al_xGa_{1-x}As$ barriers. Also shown are the possible paths of dark current electrons and photocurrent electrons of the device under a bias (Bandara *et al.*, 1998b)

wells of three-quantum-well units are designed to respond at peak wavelengths of around 13, 14, and 15 μm, respectively. These quantum wells are separated by 75 Å-thick $Al_xGa_{1-x}As$ barriers. The Al mole fraction (x) of barriers throughout the structure was chosen such that the $\lambda_p = 13\,\mu m$ quantum well operates under the bound-to-quasibound conditions. The excited-state energy-level broadening has further enhanced due to overlap of the wave functions associated with the excited states of quantum wells separated by thin barriers. Energy band calculations based on a two-band model shows excited state energy levels spreading about 28 meV. An experimentally measured responsivity curve at $V_B = -3$ V bias voltage has shown broadening of the spectral response up to $\Delta\lambda \sim 5.5\,\mu m$, i.e. the full width at half maximum from 10.5–16 μm. This broadening $\Delta\lambda/\lambda_p \sim 42\%$ is about a 400% increase compared to a typical bound-to-quasibound QWIP.

Later, Nedelcu *et al.* also developed broadband QWIPs for spectrometer applications (Nedelcu *et al.*, 2010). Three QWIP layers have been specifically designed, grown, processed, and characterized for broadband applications. For the active layer, two very-different design approaches have been tested. The first one is based on the implementation of different quantum wells (QW) into the active layer. Each QW has a different peak absorption wavelength. Consequently the total absorption spectrum is given by the sum of the individual absorption peaks. For this study, four different QW types with nominal peak absorption wavelengths at 11.5 μm, 12.5 μm, 13.7 μm, and 14.7 μm have been used. The design has been optimized in order to achieve spectral shapes robust with respect to the temperature and applied bias. The dark current has not been optimized, as the main concern here was the achievement of a broadband

response. The second design approach was based on the replacement of individual quantum wells by short superlattices. Each superlattice is made of four coupled-quantum wells, separated by AlGaAs barriers that were only 6–7 nm thick. The superlattices are separated from one another by 36 nm-thick barriers. In order to achieve a truly broadband absorption spectrum, a specific optical coupling scheme is required and it's discussed in the "light coupling" section of this chapter.

2.6. n-Doped Bound-to-Bound Miniband QWIPs

The superlattice miniband detector uses the concept of infrared photoexcitation between the minibands (ground state and first excited state) and transport of these photoexcited electrons along the excited-state miniband. When the carrier de Broglie wavelength becomes comparable to the barrier thickness of the superlattice, the wave functions of the individual wells tend to overlap because of tunneling, and the energy minibands are formed. The miniband occurs when the bias voltage across one period of the superlattice becomes smaller than the miniband width (Capasso *et al.*, 1986).

Experimental work on infrared detectors involving the miniband concept was initially carried out by Kastalsky *et al.* (1988). The spectral response of this GaAs/AlGaAs detector was in the range 3.6–6.3 μm and this indicated that low-noise infrared detection was feasible without the use of external bias. O *et al.* (1990) reported experimental observations and related theoretical analysis for this type of detectors with absorption peak in the LWIR spectral range (8–12 μm). Both these detectors consist of a bound-to-bound miniband transition (i.e., two minibands below the top of the barrier) and a graded barrier between the superlattice and the collector layer as a blocking barrier for ground-state miniband tunneling dark current.

In order to further reduce the ground-state miniband tunneling dark current, Bandara *et al.* (1992) used a square-step barrier at the end of the superlattice. This structure, illustrated in Fig. 2.7A, was grown by MBE and consists of 50 periods of 90 Å GaAs quantum wells and 45 Å $Al_{0.21}Ga_{0.79}As$ barriers. A 600 Å-$Al_{0.15}Ga_{0.85}As$ blocking layer was designed in such a way that it has two minibands below the top of the barrier, with the top of the step blocking barrier being lower than the bottom of the first excited state miniband, but higher than the top of the ground state miniband. The spectral photoresponse was measured at 20 K with a 240 mV bias voltage across the detector and at 60 K with a 200 mV bias voltage. The experimental response band of this detector was in the VLWIR range, with peak response at 14.5 μm. The rapid fall-off in the photocurrent at higher bias voltage values was observed and attributed to the progressive decoupling

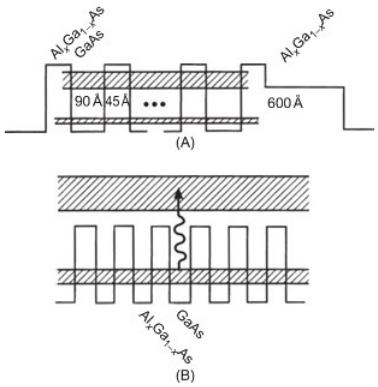

FIGURE 2.7 (A) Parameters and band diagram for LWIR GaAs / $Al_xGa_{1-x}As$ superlattice miniband detector with $\lambda_c \sim 15\,\mu m$. (Bandara *et al.*, 1988); (B) device structure of bound-to-continuum miniband (Gunapala *et al.*, 1991b)

of the miniband as well as the rapid decrease in the impedance of the detector.

The peak responsivity of this detector at 20 K and 60 K are 97 and 86 mA/W for unpolarized light. Based on these values and noise measurements, the estimated detectivity at 20 K and 60 K are 1.5×10^9 and 9×10^8 cm$\sqrt{\text{Hz}}$/W, respectively. Although this detector operates under a modest bias and power conditions, the demonstrated detectivity is relatively lower than the responsivity of usual QWIPs. This is mainly due to the lower collection efficiency. Although there is enough absorption between minibands, only the photoexcited electrons in few quantum wells near the collector contact contribute to the photocurrent.

2.7. n-Doped Bound-to-Continuum Miniband QWIPs

It is anticipated that placing the excited state miniband in the continuum levels would improve the transportation of the photoexcited electrons, i.e., responsivity of the detector. This is same as in the case of the wide barrier bound-to-continuum detectors discussed previously. A detector based on the photoexcitation from a single miniband below the top of the barriers to one above the top of the barriers is expected to show

a higher performance. Gunapala *et al.* (1991b) proposed and demonstrated this type of bound-to-continuum miniband photoconductor based on GaAs/$Al_xGa_{1-x}As$ superlattice operating in the 5–9 μm spectral range. Their structure shows more than an order of magnitude improvement in electron transport and detector performance, compared with the previous bound-to-bound state miniband detectors.

Device structures (as shown in Fig. 2.7B) studied by Gunapala *et al.* (1991b) consisted of 100 periods of GaAs quantum wells of either $L_b = 30$ Å or $L_b = 45$ Å barriers of $Al_{0.28}Ga_{0.72}As$, and $L_w = 40$ Å GaAs wells (doped $N_D = 1 \times 10^{18}\,cm^{-3}$) sandwiched between the doped GaAs contact layers. The absolute values for the peak absorption coefficients are $\alpha = 3100\,cm^{-1}$ and $\alpha = 1800\,cm^{-1}$ for the $L_b = 30$ and 45 Å structures, respectively. Structures with a narrower barrier ($L_b = 30$ Å) have a higher peak absorption coefficient as well as a broader spectrum, resulting in significantly larger integrated absorption strength. Also, the dark current of this structure ($L_b = 30$ Å) is much larger than that of the other ($L_b = 45$ Å) structure.

Detectivities at peak wavelength for the above miniband detectors were calculated using the measured responsivities and the dark currents. For the $L_b = 30$ Å structure, the result was $D^* = 2.5 \times 10^9$ and $5.4 \times 10^{11}\,cm\sqrt{Hz}/W$ for $T = 77$ and 4 K at −80 mV bias. For $L_b = 45$ Å structure, they obtained $D^* = 2.0 \times 10^9$ and $2.0 \times 10^{10}\,cm\sqrt{Hz}/W$ for $T = 77$ and 4 K at −300 mV bias. These values are significantly higher than the previous bound-to-bound miniband results. Although the responsivity is improved by placing the excited state in the continuum, it also increases the thermionic dark current because of the lower barrier height. This fact is more critical for LWIR detectors because the photoexcitation energy becomes even smaller, i.e., the detector operating temperature will be lowered.

2.8. n-Doped Bound-to-Miniband QWIPs

Yu and Li (1991a) and Yu *et al.* (1991b) proposed and demonstrated a miniband transport QWIP which contained two bound states with higher energy level being resonance with the ground state miniband in the superlattice barrier. (see Fig. 2.8A). In this approach, infrared radiation is absorbed in the doped quantum wells, exciting an electron into the miniband and transporting it in the miniband until it is collected or recaptured into another quantum well. Thus, the operation of this miniband QWIP is analogous to that of a weakly-coupled MQW bound-to-continuum QWIP. In this device structure, the continuum states above the barriers are replaced by the miniband of the superlattice barriers. These miniband QWIPs show lower photoconductive gain than the bound-to-continuum QWIPs because the photoexcited electron transport occurs in the miniband where electrons have to transport through many thin

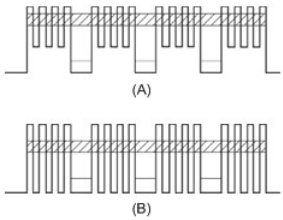

FIGURE 2.8 Band diagrams for (A) bound-to-miniband; (B) step bound-to-miniband QWIP structures. (Levine, 1993)

heterobarriers resulting in lower mobility. Bandwidth of the absorption spectrum is controlled by the position of the miniband, relative to the barrier threshold, as well as the width of the miniband, which is exponentially dependent on the thickness of the superlattice barriers. Faska *et al.* (1992) adopted this bound-to-miniband approach and demonstrated excellent LWIR images from a 256×256 focal plane array (FPA) camera. These bound-to-miniband QWIPs have been demonstrated using a $GaAs/Al_xGa_{1-x}As$ material system. In order to further improve the performance (by decreasing the dark current) of these miniband QWIPs, Yu *et al.* (1992) proposed a step bound-to-miniband QWIP which is shown in Fig. 2.8B. This structure consists of $GaAs/Al_xGa_{1-x}As$ superlattice barriers and $In_{0.07}Ga_{0.93}As$- strained quantum wells, which are deeper than the superlattice barrier wells, as shown in Fig. 2.8B (Li *et al.*, 1993).

Dark Current

Improving QWIP performance depends largely on minimizing the dark current that flows through a biased detector with no photons impinging on it. In QWIPs, the dark current originates from three different mechanisms.[4-6] The dark current arising from the first process is due to quantum mechanical tunneling from well to well through the $Al_xGa_{1-x}As$ barriers (sequential tunneling). This process is independent of temperature. Sequential tunneling dominates the dark current at very low temperatures (<30 K). The second mechanism is thermally assisted tunneling which involves a thermal excitation and tunneling through the tip of the barrier into the continuum energy levels. This process governs the dark current at medium temperatures. The third mechanism is classical thermionic emission and it dominates the dark current at higher temperatures (>55 K for 9 μm cutoff Q WI Ps). The thermal generation rate associated with this current depends on the well doping density and the life time of the carriers which will be determined by the thickness of the $Al_xGa_{1-x}As$ barriers. Consequently, for QWIPs operating at higher temperatures the last mechanism is the major source of dark current[4,6]

In order to optimize the performance of the QWIP, a *bound-to-quasibound* quantum well was developed by placing the first excited state exactly at the well top as shown in Fig. 2. Dropping the first excited state to the well top causes the barrier to thermionic emission (roughly the energy height from the ground state to the well top) to be - 10-15 meV more than that of the bound-to-continuum (the first excited state lies in the continuum energy band above the well top) QWIP.[4] The dark current-voltage curve of the 15 μm peaked bound-to-quasibound QWIP is shown in Fig. 2. This compares well with the experimentally observed more than 10 factor drop compare to the *bound-to-continuum Q* WI P having the same peak wavelength.

Spectral Response

Unlike the responsivity spectrums of intrinsic infrared detectors, the responsivity spectrums of QWIPs are much narrow and sharper due to their resonance intersubband absorption.[1,2] The normalized responsivity spectra $R(\lambda)$ are given in Fig. 3, where we see that the *bound* and *quasibound* excited state QWIPs are much narrower $\Delta\lambda/\lambda$ - 10% than the *continuum* QWIPs $\Delta\lambda/\lambda$ = 24 o/o. This is due to the fact that when the excited state is placed in the continuum band above the barrier, the energy width associated with the state becomes wider, spectral band width becomes wider. Spectral band width of these QWIPs can be further increased by increasing the carrier density and by slightly varying the parameters of the quantum wells of the multi-quantum well structure.' See Figure 4. This device structure involved several repeated layers of three different GaAs/$Al_xGa_{1-x}As$ quantum wells separated thick $Al_xGa_{1-x}As$ barriers. The thickness of the GaAs layer of these three quantum wells ate designed to response at peak wavelengths 13.5 pm, 14.3 μm and 15.5 μm respectively. These measurements show broadening of the spectral response up to $\Delta\lambda$ - 6 μm, i.e. the full width at the half maximum from 13.2 -16.6 pm. This broadening $\Delta\lambda/\lambda_p$ - 46% is more than 400 % increase comparing to a typical bound-to-quasibound QWIP. This band width can be tuned to a desired value by varying the structure parameters.[7]

The absolute peak responsivity R_p can be written in terms of quantum efficiency η and photoconductive gain g as $R_p = (e/h\ v)\ \eta g$. The bias dependence of R_p is shown in Fig. 5. Note that at low bias the responsivity is nearly linearly dependent on bias and it saturates at high bias. This saturation occurs due to the saturation of carrier drift velocity. The responsivity of more *bound-to-bound* samples has a significantly different shape. The responsivity does not start out linearly with bias but is in fact zero for finite bias. That is, there is a zero bias offset of more than 1 V, due to the necessity of field assisted tunneling for the photoexcited carrier to escape from the well.

At low operating bias voltages, responsivity spectrum of bound-to-bound QWIPs show additional peaks due to resonance energy levels of potential barriers. See Figure 6. Although the absorption between ground state and barrier resonance levels are much smaller than that of the ground and first excited state, at lower bias voltages escape probability of the photoexcited

electrons at the bounded first excited state is much smaller. When the bias the escape probability of the photoexcited electrons at the excited state (bounded to the well) also increases. Thus the peak associates with the bound to excited transition becomes dominant in the spectrum. Also, due to the same reason, bound-to-continuum QWIPs do not show any responsivity peaks associated with barrier resonances.

Light Coupling

QWIPs do not absorb radiation incident normal to the surface since the light polarization must have an electric field component normal to the superlattice (growth direction) to be absorbed by the confined carriers [1,2]. When the incoming light contains no polarization component along the growth direction, the matrix element of the interaction vanishes (i.e., $\vec{\varepsilon}.\vec{p}_z=0$ where $\vec{\varepsilon}$ is the polarization and $\vec{p}_z$ is the momentum along z direction). As a consequence, these detectors have to be illuminated through a 45° polished facet [1,2]. Clearly, this illumination scheme limits the configuration of detectors to linear arrays and single elements. For imaging, it is necessary to be able to couple light uniformly to two dimensional arrays of these detectors.

Several different monolithic grating structures, such as linear gratings", two-dimensional (2-D) periodic gratings[10-12], and random-reflectors [13,14] have been demonstrated for efficient light coupling to QWIPS, and has made two dimensional QWIP imaging arrays' feasible. These gratings deflect the incoming light away from the direction normal to the surface, enabling intersubband absorption. These gratings were made of metal on top of each detector or crystallographically etched through a cap layer on top of the MQW structure. Normal incident light-coupling efficiency comparable to the light coupling efficiency of a 45° polished facet illumination was demonstrated using linear gratings [8,9].

Detailed theoretical analysis [11] has been carried out on both linear and 2-D periodic gratings for QWIPs. In 2-D gratings, the periodicity of the grating repeats in two perpendicular directions on the detector plane, leading to the absorption of both polarizations of incident IR radiation. Also, experiments have been carried out for two-dimensional grating coupled QWIP detectors designed for wavelengths λ - 9 μm[10] and λ - 16 - 17 μm[14]. A factor of 2-3

responsivity enhancement relative to the standard 45° polished facet illumination was observed for large area mesas (500 pm x 500 μm) with total internal reflection optical cavity which can be created with an additional AlGaAs layer [10,11] or with a thinned substrate [12]. This optical cavity is responsible for about an extra enhancement factor of two due to the total internal reflection from the AlGaAs layer or from the thinned substrate (Fig. 7).

Random reflectors have demonstrated excellent optical coupling for individual QWIPs as well as for large area focal plane arrays[13,14]. It has been shown that many more passes of IR light (Fig. 7), and significantly higher absorption, can be achieved with a randomly roughened reflecting surface. By careful design of surface texture randomization (with three level random reflector), an enhancement factor-of-eight in responsivity compared to 45° illumination was demonstrated experimental y [13]. The random structure on top of the detector prevents the light from being diffracted normally backward after the second bounce as happens in the case of 2-D periodic grating. See Fig. 7. Naturally, thinning down the substrate enables more bounces of light and therefore higher responsivity[13].

All these gratings were fabricated on the detectors by using standard photolithography and selective dry etching. The advantage of the photolithograpic process is its ability to accurately control the feature size and to preserve the pixel-to-pixel uniformity, which is a prerequisite for high-sensitivity imaging focal plane array. However the resolution of the photolithography and the accuracy of etching processes become key issues in producing smaller grating feature sizes. These feature sizes are proportionally scaled with the peak response wavelength of the QWIP. It is important to note that for any given wavelength the random grating requires much smaller feature sizes than two dimensional periodic gratings. [15] The minimum feature size of the random reflectors of 15 μm and 9 μm cutoff FPAs were 1.25 and 0.6 μm respectively.[15] Thus, the random reflectors of the 9 μm cutoff FPA were less sharp and had fewer scattering centers compared to random reflectors of the 15 μm cutoff FPA and this is due to the difficulties associated with sub-micron photolithography. These less sharp features in random gratings lowered the light coupling efficiency than expected. Thus, it could be advantageous to utilize a 2-D periodic grating for light coupling in shorter wavelength QWIPs.

SUMMARY

In summary, QWIPs afford greater flexibility than the usual extrinsically doped semiconductor IR detectors because the wavelength of the peak response and cutoff can be continuously tailored by varying layer thickness (well width), barrier composition (barrier height), and carrier density (well doping density). The $GaAs/Al_xGa_{1-x}As$ material system allows the quantum well parameters to be varied over a range wide enough to enable light detection at any wavelength range between 6-20 pm. The spectral band width of these detectors can be tuned from narrow ($\Delta\lambda/\lambda$ -10 %) to wide ($\Delta\lambda/\lambda$ - 40 %) allowing various applications. Also, we have observed an enhancement factor of three due to 2D periodic grating fabricated on QWIP

structure. Variation of the enhancement factor with groove depth and feature size of the grating can be theoretically explained. However the resolution of the photolithography and accuracy of the etching become key issues in producing smaller grating feature sizes especially in shorter wavelengths. Unlike random reflectors the light coupling efficiency of two dimensional (2-D) gratings strongly depends on the wavelength and thus exhibits narrow band width spectral responses.

ACKNOWLEDGMENTS

The research described in this paper was performed by the Center for Space Microelectronics Technology, Jet Propulsion Laboratory, California Institute of Technology, and was sponsored by the National Aeronautics and Space Administration, Office of Space Science,

References

1. S. D. Gunapala and K. M. S. V. Bandara, in *Physics of Thin Films*, edited by M. H. Francombe and J. L. Vossen, Vol. 21, pp. 113-237, Academic Press, NY, 1995.
2. B. F. Levine, J. Appl. Phys. 74, RI (1993).
2. K. K. Choi, J. Appl. Phys. 73, 5230 (1993).
4. B. F. Levine, C. G. Bethea, G. Hasnain, V. O. Shen, E. Pelve, R. R. Abbott, and S. J. Hsieh, Appl. Phys. Lett., 56,851 (1990).
5. E. Pelve, F. Beltram, C. G. Bethea, B. F. Levine, V. O. Shen, S. J. Hsieh, R. R. Abbott, J. Appl. Phys. 66,5656 (1989).
6 S. D. Gunapala, J. K. Liu, J. S. Park, M. Sundaram, C. A. Shott, T. Helter, T. L. Lin, S. T. Massie, P. D. Maker, R. E. Muller, and G. Sarusi, IEEE Trans. Ele. Devices, vol. 44, 45-59(1997).
7. S. V. Bandara, S. D. Gunapala, J. K. Liu, J. Mumolo, E. Luong, W. Hong and D. K. Sengupta, to be published.
8. K. W. Goossen, S. A. Lyon, J. Appl. Phys, vol. 63. 5149(1988).

9. G. Hansain, B. F. Levine, C'. G. Bethea, R. A. Logan, J. Walker, and R. J. Malik, Appl. Phys. lett., vol. 54,2515 (1989).
10. J. Y. Andersson and L. Lundqvist, Appl. Phys, Lett. vol. 59, 857(1 991).
11. J. Y. Andersson, L. Lundqvist and Z. F. Paska, J. Appl. Phys. vol. 71,3600 (1991).
12. G. Sarusi, B. F. Levine, S. J. Pearton, K. M. S. V. Bandara, R. E. Leibenguth, and J. Y. Andersson J. Appl. Phys., vol. 76, 4989(1994).
13. B. Xing, and H. C, Liu, J. Appl. Phys., vol. 80, 1214 (1996).
14. G. Sarusi, B. F. Levine, S. J. Pearton, K. M. S. V. Bandara, and R. E. Leibenguth, *Appl. Phys. Let/.*, vol. 64, pp. 960-962,(1994).
15, S. Bandara, S. Gunapala, J. Liu, W. Hong and J. Park, SPIE Vol. 2999, 103 (1 997).

Figure Captions

Fig. 2 Comparison of dark currents of bound-to-continuum and bound-to-quasibound QWIPs as a function of bias voltage at temperature T = 55 K.

Fig. 3 Spectral band width variation of QWIPs with bound-to-bound and bound-to-continuum transitions.

Fig. 4 Normalized spectral responsivity of broad-band QWIPs.

Fig.6. Normalized spectral responsivity ofa bound-to-bound QWIPs showing additional peak due to barrier resonance at lower bias voltages.

Fig. 7 (a) Schematic side view of a thin QWIP pixel with a random grating reflector. Ideally all the radiation is trapped except for a small fraction which escapes through the escape cone. (b) Schematic diagram of 2-D periodic grating specifications. The grating features are spaced periodically along the x and y directions.

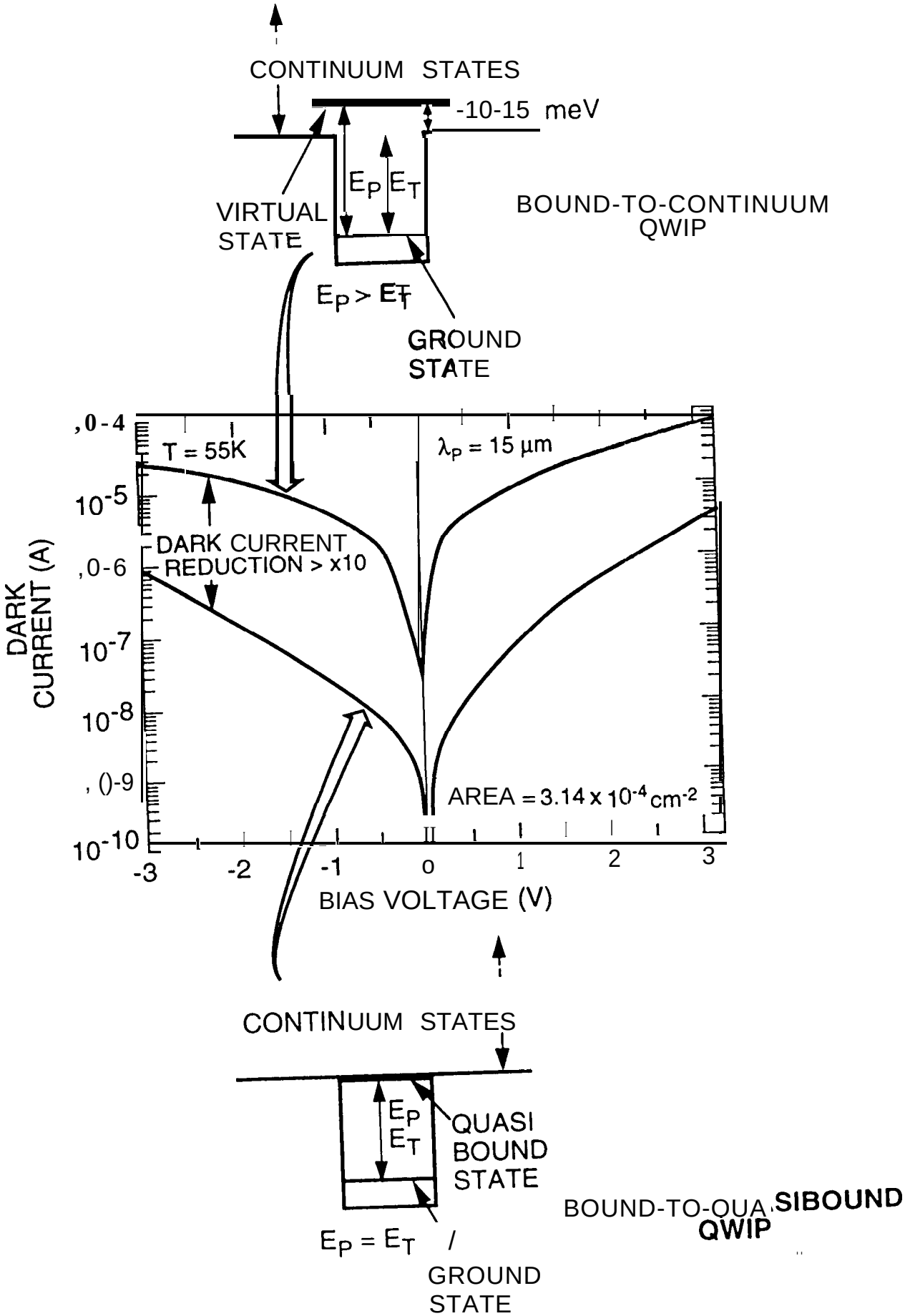
CONTINUUM STATES
-10-15 meV
E_P E_T
VIRTUAL STATE
BOUND-TO-CONTINUUM QWIP
$E_P > E_T$
GROUND STATE
T = 55K
λ_P = 15 µm
DARK CURRENT REDUCTION > x10
DARK CURRENT (A)
10^{-5}
10^{-7}
10^{-8}
10^{-10}
AREA = 3.14 x 10^{-4} cm^{-2}
-3
-2
-1
0
1
2
3
BIAS VOLTAGE (V)
CONTINUUM STATES
E_P
E_T
QUASI BOUND STATE
BOUND-TO-QUASIBOUND QWIP
$E_P = E_T$
GROUND STATE

Fig 2

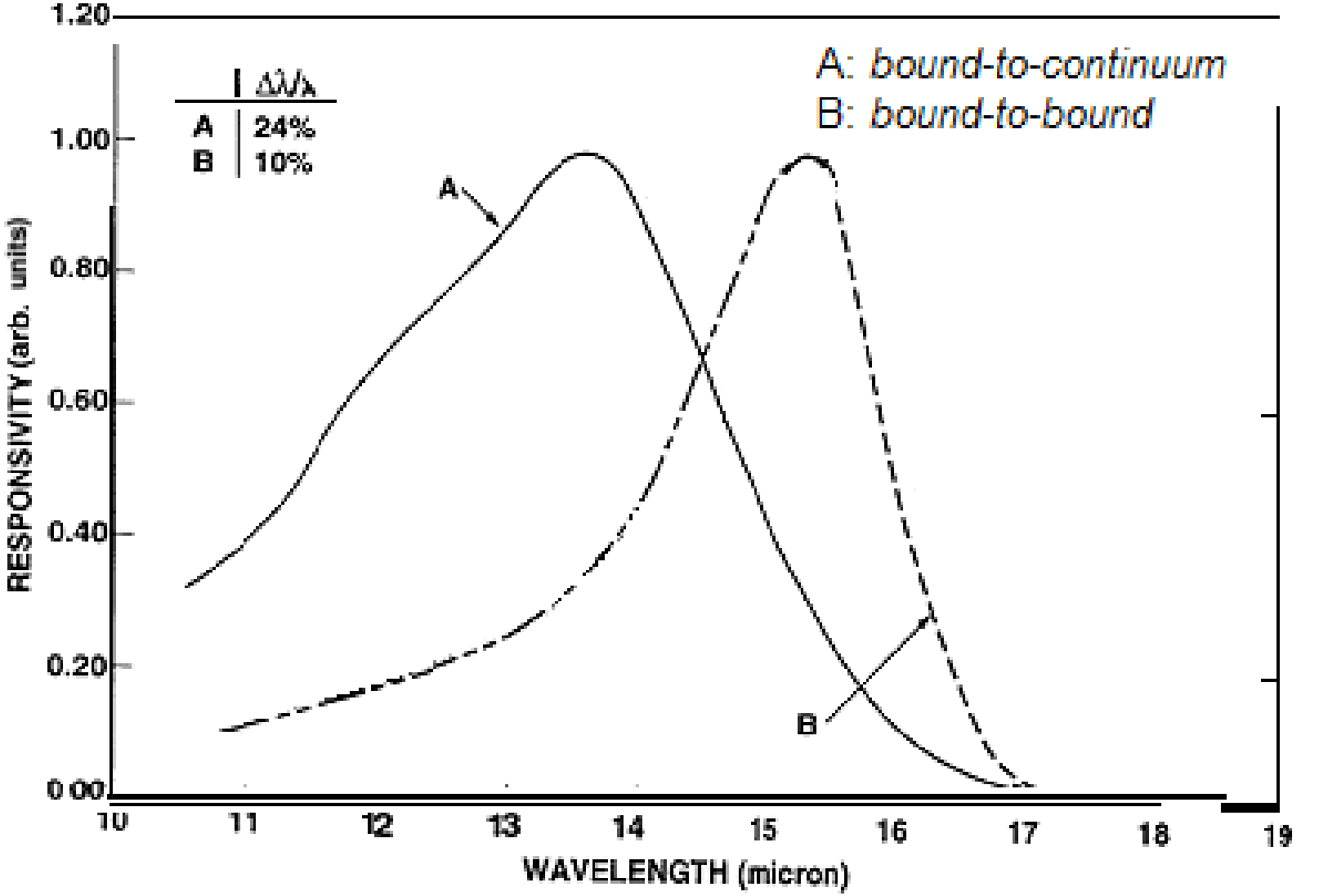
1.20
1.00
0.80
0.60
0.40
0.20
0.00
RESPONSIVITY (arb. units)
Δλ/λ
A 24%
B 10%
A: bound-to-continuum
B: bound-to-bound
A
B
10
11
12
13
14
15
16
17
18
19
WAVELENGTH (micron)

Fig 3

BROAD-BAND QWIP

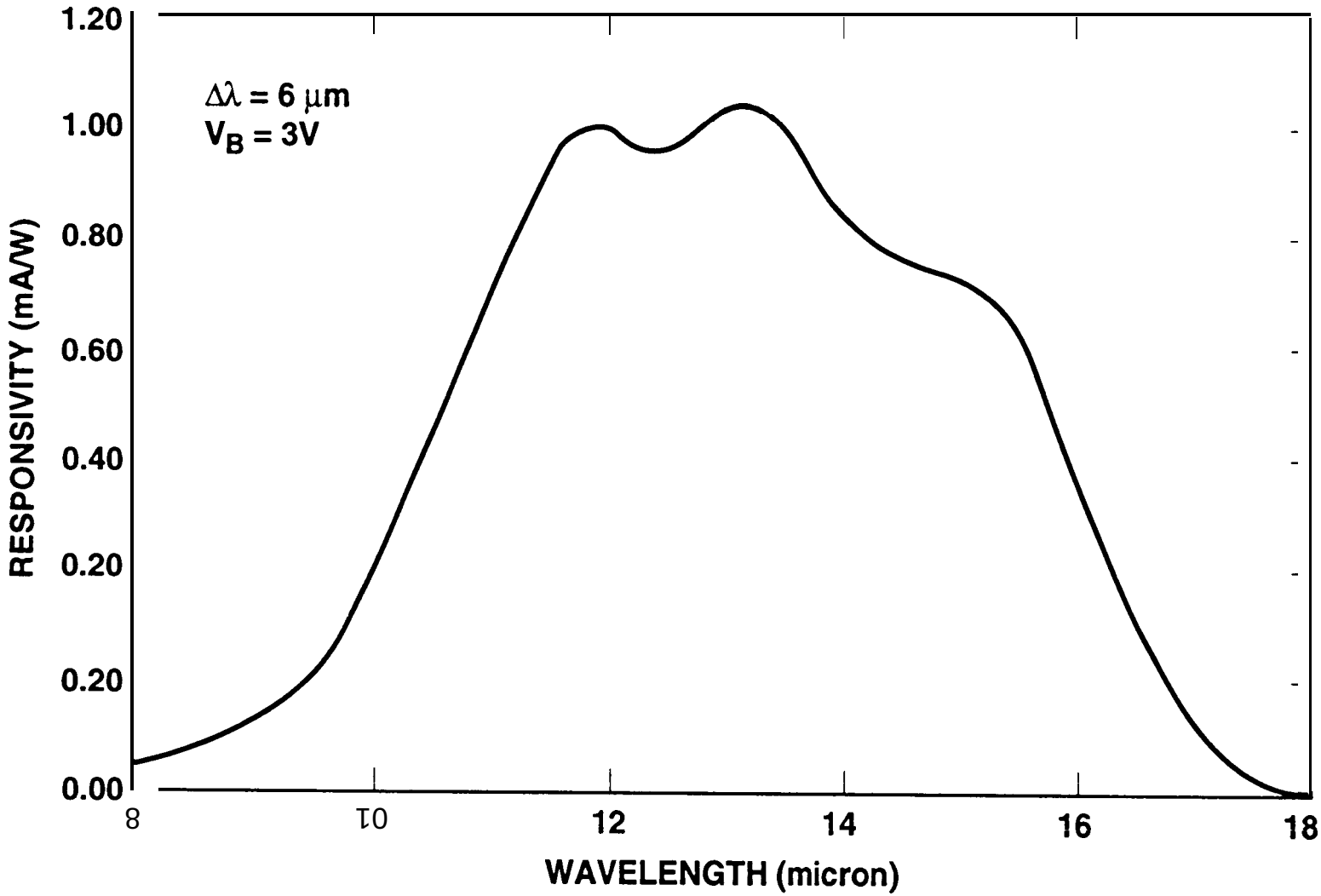

Fig 4

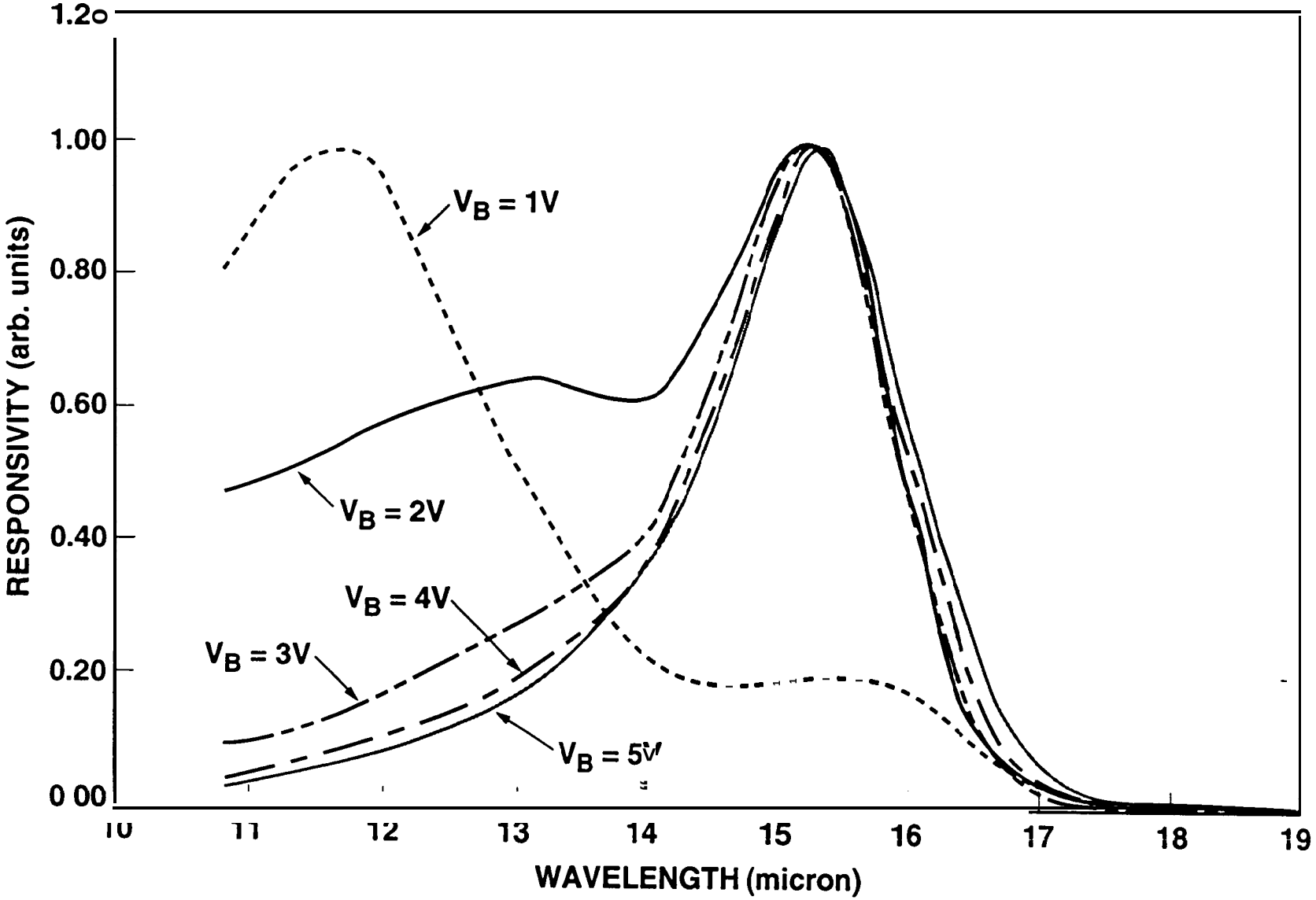
1.2o
1.00
0.80
0.60
0.40
0.20
0 00
RESPONSIVITY (arb. units)
V_B = 1V
V_B = 2V
V_B = 4V
V_B = 3V
V_B = 5V
10
11
12
13
14
15
16
17
18
19
WAVELENGTH (micron)

Fig 6

BD-04

(a)

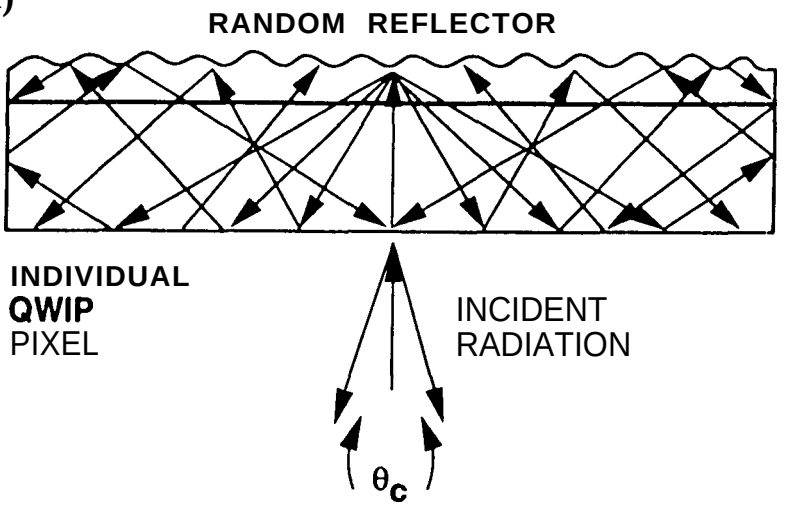
RANDOM REFLECTOR
INDIVIDUAL
QWIP
PIXEL
INCIDENT
RADIATION
θ_c

(b)

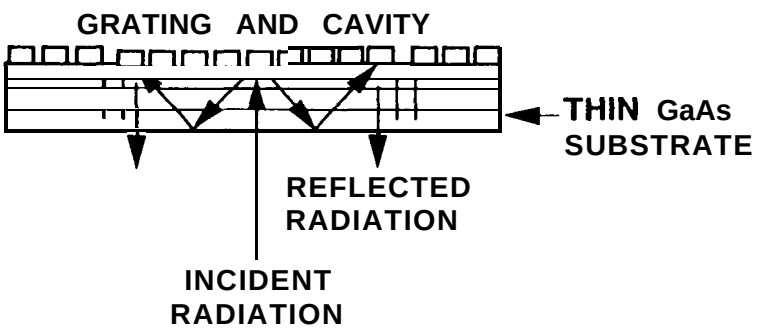
2D GRATING
GRATING AND CAVITY
THIN GaAs
SUBSTRATE
REFLECTED
RADIATION
INCIDENT
RADIATION

BD-07

Fig 7

Applicazioni visione IR

Passive IR Imaging

By Dr. Arnold Goldberg

Arnold Goldberg, University of Maryland alumnus and Team Leader of the Passive IR Imaging Team of the EO/IR Technology Branch at Army Research Laboratory talks about IR Imaging and a career with the Federal government.

Introduction

I received my Ph. D. in Physics from the University of Maryland in 1996 but it was not by the "usual" method. I received my B.S. in Physics in 1981 from Maryland and I was fortunate enough to get a job as a research technician at Martin Marietta Laboratories (MML) in Baltimore. It was the corporate research and development (R&D) lab for Martin Marietta, a major defense contractor. I worked in the Advanced Infrared Technologies department where my initial job was to develop fabrication process for infrared (IR) photodiodes. Later on, I moved into device testing. During the period from 1983 to 1987 I went to school in the evenings to earn an M. S. in Applied Physics from Johns Hopkins University. From 1988 through 1996, I worked on my Ph. D. under Professor Robert Anderson at the University of Maryland. My thesis research was on electron transport in semiconductor superlattices.

In early 1995, just as I was finishing the experiments, Martin Marietta and Lockheed merged to form Lockheed Martin. A few months after that, management decided that they no longer needed a corporate research lab and Martin Marietta Laboratories was closed. By this time I had worked my way up from technician to scientist and I was supervising the laboratory and field testing of IR focal plane array (FPA) imagers. My group was transferred to a facility in Nashua, New Hampshire but there was no way I was going to move there. Again I was very fortunate in that a former colleague was able to get me - and a number of other laid off MML employees - jobs as contractors at the Army Research Laboratory (ARL) in Adelphi, MD (just 5 minutes from College

Park). I was actually an employee of the University of Maryland under a co-operative agreement with the Army. I was able to finish my thesis and to be given the responsibility of setting up a new IR test facility at ARL.

In January of 1999 I was hired as a Federal employee and now I am the Team Leader of the Passive IR Imaging Team of the EO/IR Technology Branch at ARL. I enjoy working for the Government because it allows me the freedom to be completely objective in my work. In my experience working 14 years in industry, there was always pressure to make the things we were working on look as good as possible and to continually advocate whatever technology we thought was best. There are several interesting projects that I am currently working on. I will try to give a short overview on what they are.

The United States Army relies heavily on infrared IR for night vision, target acquisition, and fire control. Advanced IR sensor systems allow operations to be conducted at night and under adverse weather conditions. At ARL, we are conducting research aimed at advancing the state-of-the-art in IR imaging sensor technology so that the vehicles of the Army's Future Combat System (FCS) will be able to identify hostile targets at ranges beyond those at which an enemy would detect our vehicle.

There has also been a rapid growth in the commercial use of IR sensors for such applications as medical diagnostics, industrial process monitoring and control, physical security, and firefighting. In addition, IR camera systems have begun to be installed in automobiles to enhance driver night vision (available on a Cadillac as a $2000 option). The military and commercial IR markets are expanding and there is a need for enhanced performance and lower cost of these sensors.

What is IR?

Before I get into the new technologies on which we at ARL are working in this area, I will give a short background on the IR. The IR portion of the electromagnetic spectrum is generally defined as those wavelengths just beyond those of visible light (about 700 nm) to wavelengths of 100 m. At longer wavelengths the IR blends into the "millimeter wave" spectrum.

A combination of circumstances defines the regions of the spectrum where most IR sensors are designed to operate. It turns out that the Earth's atmosphere is relatively transparent in only certain spectral "windows" as shown in Figure 1. These three spectral bands in which the atmosphere is relatively transparent are called short-wave IR (SWIR 0.7 - 2 m), mid-wave IR (MWIR 3 - 5 m), and long-wave IR (LWIR 8 - 14 m). It also turns out that the wavelength of maximum blackbody emission for objects near room temperature (300 K) is 10 m, right in the middle of the LWIR band. The wavelength of maximum thermal contrast, the wavelength at which the derivative of the Planck radiation function is maximal, for a blackbody at room temperature is in the MWIR band. Therefore, most IR sensor systems have been designed to work in either of these bands. There are a number of different semiconductor materials that may be used for IR detection. Entire books have been devoted to that subject so I won't go into that here.

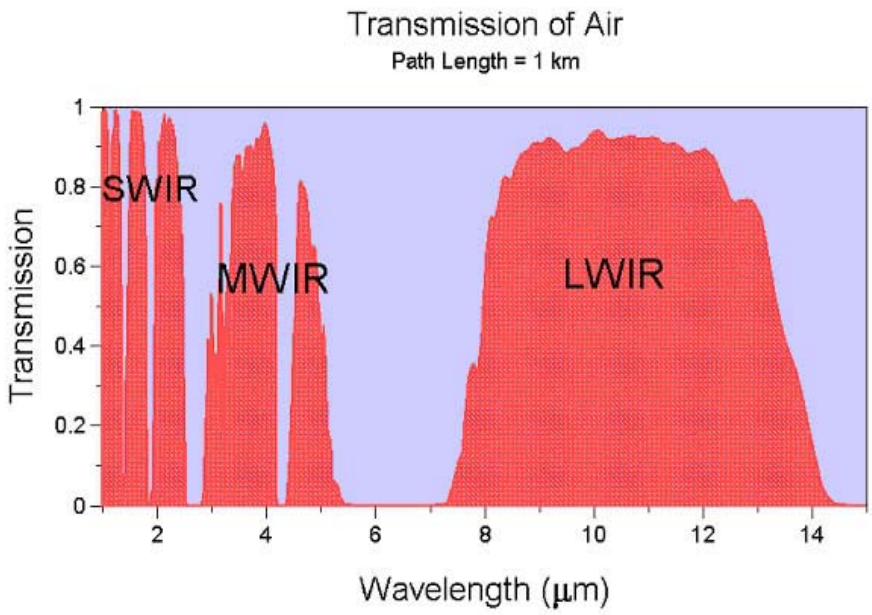

Figure 1. Atmospheric transmission in the infrared showing the principal transmission windows.

Army Research in IR

Under ARL's Federated Laboratory program which lasted from 1996 - 2001 and its successor the Collaborative Technology alliance (2001 - 2006) ARL has teamed with a consortium of academic and industrial partners to research areas of interest to the Army. IR imaging is one of these areas and the particular focus of that program was to develop IR detector arrays that can see in both the MWIR and LWIR atmospheric transmission windows independently yet simultaneously, a dual-band IR FPA. Such an FPA would allow operation in a wider range of ambient conditions (fog, smoke, etc.) than a single-band FPA and holds the promise of being able to detect targets in cluttered scenes better than a single-band FPA. To produce a dual-band FPA the detectors sensitive to LWIR and MWIR light had to be stacked on top of each other and contacted independently. This concept presented serious challenges to the material growth and processing capabilities for the IR FPA foundries as well as for the read-out integrated circuit (ROIC, also called a multiplexer) design.

We at ARL worked closely with Lockheed Martin Sanders (now part of BAE Systems North America) to produce dual-band FPAs using the GaAs/AlGaAs quantum well infrared photodetector (QWIP) technology and with DRS Infrared Technology to produce dual-band FPAs using HgCdTe material. The FPAs were delivered to ARL and I characterized their performance in the laboratory; the results were published in the literature.

To demonstrate the usefulness of dual-band IR imaging, Figure 2 shows an image taken with the QWIP dual-band IR FPA of a coffee mug (filled with hot coffee) that I got from a trade show from nFocus, a laser company. The mug has printed lettering with the company's logo as well as lettering with words like "optics" bead-blasted into the

surface. The bead-blasted lettering shows up well in the LWIR image because the rough surface enhances the local emissivity. LWIR emission is very sensitive to the surface roughness. On the other hand, the printed lettering suppresses the MWIR emission because it is highly reflective in that band. Thus materials at equal temperatures can have very different IR signatures. We hope to exploit this effect to defeat camouflage of other deception techniques. The right image in Figure 2 is a color fusion of the individual LWIR and MWIR images. The LWIR image has been mapped to shades of red and the MWIR image to shades of cyan (opponent colors). In the resulting fused image, pixels where LWIR emission dominates are shaded red and those where MWIR is dominant are shades of cyan. Those in which the MWIR and LWIR emission are approximately equal are shades of gray. The fused image not only shows the details of the mug that were apparent in the individual images, but also the background objects on the table that were too dim to see in the individual images. Thus, by fusing the LWIR and MWIR images into a single image, more information from the seen can be visualized than with a single-band image.

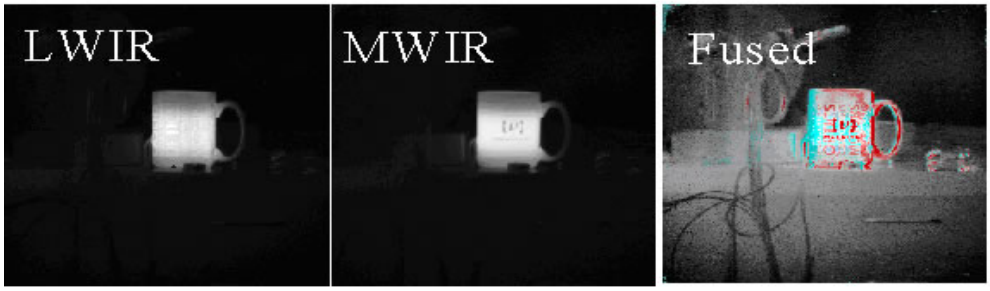

Figure 2. Image of a coffee mug with bead-blasted and printed lettering. At right is a color image fusion of the LWIR and MWIR images.

We have also inserted the dual-band FPAs into camera systems and taken them to field tests against military targets. An example of an image in the field is shown in Figure 3. At first glance the LWIR and MWIR images appear very similar but the fused image points out the significant differences between them. The concrete slab at the right of each image is highly emissive in the MWIR band and therefore shows up as bright cyan in the fused image. Conversely, the dirt road emits mores strongly in the LWIR band and appears red in the fused image. The exhaust plume in back of the tank emits strongly in the MWIR (especially farther out from the vehicle) and is therefore acquires a blue shading in the fused image. More results of field imaging using these dual-band FPAs can be found in the literature.

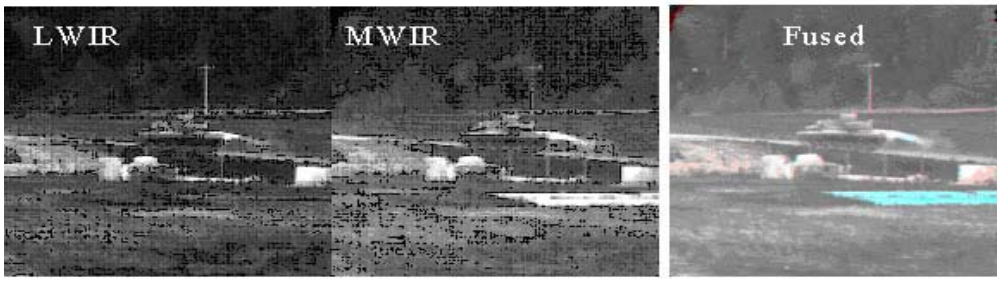

Figure 3. Dual-band image of an M60 tank taken with a dual-band IR FPA. At right is a color fusion of the individual images .

Another application of dual-band IR imaging is detection of buried mines. It has been shown that the disturbed soil associated with buried mines has high emissivity in a narrow portion of the LWIR spectrum relative to undisturbed soil. Other parts of the LWIR spectrum show little or no effect of the disturbance. We have developed a dual-band LWIR FPA to search for this effect. The FPA was installed in a camera system and taken to a simulated mine field at Ft. A. P. Hill, VA. Figure 4 shows some of the results of this test. The IR band 1 was designed to see the disturbed soil feature described above. Band 2 was designed to see the part of the LWIR spectrum that sees little effect of soil disturbance. The resulting image fusion at the bottom of Figure 4 is a subtraction of band 2 data from band 1. Negative values were assigned to shades of blue while positive values were assigned to shades of red. The blue areas indicated disturbed soil and were exactly in the places that the simulated mines were buried. Details of this experiment have been published.

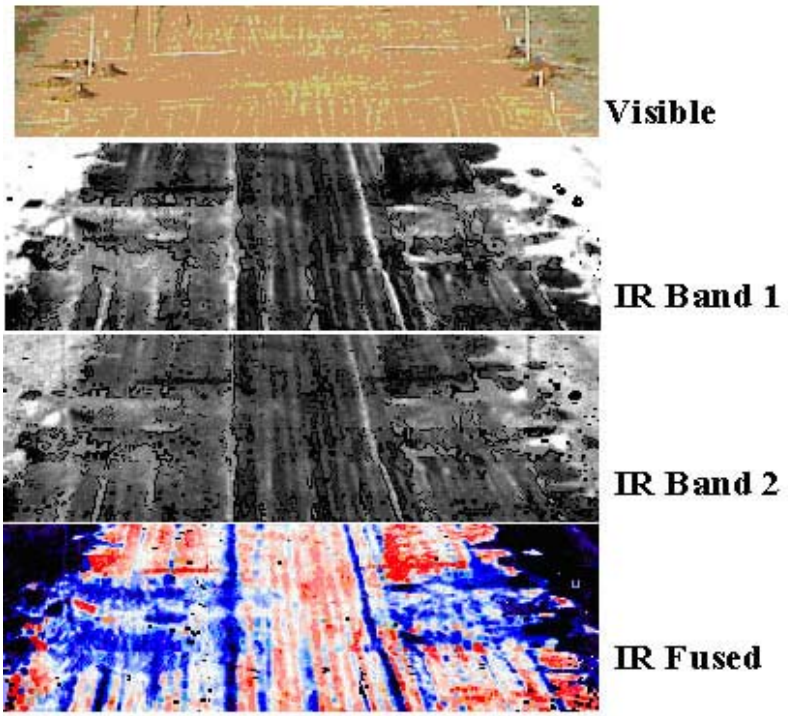

Figure 4. Dual-band LWIR imagery of a simulated mine field. At top is a visible image. At the bottom is a fused subtraction of the two IR bands. The blue shows the areas of disturbed soil that are indicative of buried mines.

These efforts at producing and evaluating dual-band IR FPAs are important steps in the ongoing effort to improve the IR imaging capability of Army systems. Eventually, it is envisioned that dual-band IR FPAs will be an important component of future Army sensor systems.

1. A. C. Goldberg, S. W. Kennerly, J. W. Little, H. K. Pollehn, T. A. Shafer, C. L. Mears, H. F. Schaake, M. Winn, M. Taylor, and P. N. Uppal, "Comparison of HgCdTe and QWIP Dual-Band Focal Plane Arrays", Proceedings of the SPIE Infrared Technology and Applications XXVII, , Vol. 4369, (2001). Revised version accepted for publication in Optical Engineering in 2002.
2. A. C. Goldberg, T. Fischer, and Z. Derzko, "Application of dual-band infrared focal plane arrays to tactical and strategic military problems", Proceedings of the SPIE Infrared Technology and Applications XXVIII, Vol. 4820, (2002).
3. A.C. Kenton, C.R. Schwartz, R. Horvath, J.N. Cederquist, L.S. Nooden, D.R. Twede, J.A. Nunez, J.A. Wright, J.W. Salisbury, K. Montavon, "Detection of Land Mines with Hyperspectral Data," Proceedings of the SPIE, Detection and Remediation Technologies for Mines and Minelike Targets IV, Vol. 3710, (1999), and refererences therein.
4. A. C. Goldberg, T. Fischer, Z. Derzko, P. Uppal, and M. Winn, "Development of a Dual-band LWIR/LWIR QWIP Focal Plane Array for Detection of Buried Land Mines", Proceedings of the SPIE, Infrared Detectors and Focal Plane Arrays VII, Vol. 4721, (2002).

Tel: 301.405.3401
1117 Physics Bldg.
University of Maryland
College Park, MD 20742

Contact the editor.
Contact the webmaster.

Image Signatures in the MWIR and LWIR Spectral Regimes

Both emissive and reflective signatures are prominent in the MWIR spectral regime, while images in the LWIR are strongly dominated by emissive signatures. In order to illustrate this difference, we have included MWIR and LWIR scenes in Figs. 2 and 3, respectively.

Reflection of sunlight from cars, in particular from their windows, gives rise to strong features in the MWIR. Emissive signatures, e. g., from a warm engine and from a person, are simultaneously visible.

In contrast, the image observed in the LWIR spectral regime is largely dominated by emissive effects, while reflective features are strongly suppressed.

Depending on the application, different signatures are of interest in infrared imaging. New system applications for QWIP-based infrared cameras will emerge since different atmospheric windows can now be exploited.

Fig. 2: IR-scene taken by a QWIP-camera operating in the MWIR spectral regime.

Fig. 3: IR-scene taken by a QWIP-camera operating in the LWIR.

Contact:
Dr. H. Schneider
Phone: +49 (0)761 5159-359
E-Mail: hschneider@iaf.fhg.de